Computer Methods in Applied Mechanics and Engineering 452 (2026) 118759

Contents lists available at ScienceDirect

Comput. Methods Appl. Mech. Engrg.

journal homepage: www.elsevier.com/locate/cma

Numerically robust local continuum damage models with softening response via convex relaxation

Celine Lauff [a], Matti Schneider [b,c,d,*], Thomas Böhlke [a]

[a] Institute of Engineering Mechanics, Karlsruhe Institute of Technology (KIT), Germany
[b] Institute of Engineering Mathematics, University of Duisburg-Essen, Germany
[c] Center for Nanointegration Duisburg-Essen (CENIDE), Germany
[d] Fraunhofer Institute for Industrial Mathematics, ITWM, Kaiserslautern, Germany

ARTICLE INFO

Keywords:
Continuum damage mechanics
Generalized standard material
Convex potentials
Convex relaxation
Optimal transport
Mesh-independent response

ABSTRACT

Continuum damage mechanics is characterized by mesh-dependent results unless specific countermeasures are taken. The most popular remedies involve introducing either nonlocality via filtering or a gradient extension for the damage variable(s). Such approaches have their limitations, e.g., they are hard to integrate into conventional finite-element codes, involve parameters that are non-trivial to determine experimentally and are incompatible with a scale transition that is both physically and mathematically sensible.

The work at hand considers an alternative route to obtain mesh-independent damage models, namely via *convex relaxation*. Such convex damage models were considered before, but they are usually not capable of representing *softening behavior*. Schwarz et al. (Continuum Mech. Thermodyn., 33, pp. 69–95, 2021) proposed such a strategy by considering the convex envelope of a rate-limited simple damage model, i.e., an isotropic damage model without tension-compression anisotropy at small strains. However, they were not able to compute the envelope explicitly and provided an approximation only.

In the work at hand, we introduce a number of conditions on the damage-degradation function which permit us to compute the convex envelope analytically for a large class of damage-degradation functions used in small-strain isotropic damage models. Interestingly, the obtained models involve a one-dimensional damaged microstructure, i.e., *damage distributions* emerge naturally. The resulting model is structurally simple and purely local, i.e., gradient-free, thermodynamically consistent and readily integrated into standard finite-element codes via traditional user subroutines.

We discuss the computational and solid mechanical aspects of the ensuing model and demonstrate its numerical robustness via dedicated computational experiments. We also show that the model permits to be homogenized by considering a representative volume element study for an industrial-scale fiber-reinforced composite.

1. Introduction

1.1. State of the art

Damage models are essential in various fields, such as engineering, materials science, and structural analysis, to predict and understand how materials or systems degrade over time under different loading conditions. These models allow simulating the

* Corresponding author.
E-mail addresses: celine.lauff@kit.edu (C. Lauff), matti.schneider@uni-due.de (M. Schneider), thomas.boehlke@kit.edu (T. Böhlke).

https://doi.org/10.1016/j.cma.2026.118759
Received 15 September 2025; Received in revised form 22 November 2025; Accepted 13 January 2026
Available online 25 January 2026

progression of damage, e.g., caused by erosion, material aging, fatigue, or fracture, and help engineers design safer, more durable structures and products. By accurately forecasting the behavior of materials under stress, damage models enable identifying potential weak spots, improving the efficiency of maintenance as well as repair strategies and reducing the risk of catastrophic failures.

To model the loss of stiffness caused by the damage progression, continuum damage mechanics [1,2] provides suitable tools based on the fundamental concepts introduced by Kachanov [3] and Rabotnov [4]. As the main assumptions, the materials are modeled as continuous and homogeneous media on the macroscale, and the damage evolution is given as an irreversible evolutionary process.

Typically, the damage degradation starts as cracks or voids on lower length scales first, then grows to defects on the macroscale and eventually leads to failure of the structure [5,6]. Depending on the underlying approach, continuum-damage models may be roughly divided into two main categories [7,8]. Micromechanics based models [7,9–11] account for the multiscale progression of the defects, and work on two scales: the continuous and homogeneous macroscale and the heterogeneous and locally discontinuous lower length scale. These models proceed as follows. First, the damage mechanisms on the lower length scale are determined. Subsequently, basic mechanics principles are employed to quantify the nonlinear response at the lower length scale accounting for the defects. Last but not least, the obtained fields are homogenized to predict the behavior on the macroscale. Due to their physical foundation, micromechanics based models are still subject to recent research and find application to several material systems and loading cases [12–15].

The second category of continuum-damage models comprises phenomenological approaches [7,8]. In contrast to micromechanics-based strategies, these models are not informed on the actual damage origin and propagation on the lower length scales, but rather provide a rational prediction based on macroscopic experiments. For the phenomenological approaches, a (set of) damage variable is selected first. Then, a thermodynamical model is postulated, linking the damage progression to an irreversible internal energy dissipation [16–20]. By construction, phenomenological approaches are strategies to describe the damage behavior directly at the macroscale. Thus, for heterogeneous materials, the stochastics at lower length scales are not taken into consideration. However, this limitation may be overcome by starting at the lower length scale and assigning to each component a phenomenological material model individually, and then homogenizing [21,22]. For such a phenomenological multiscale strategy, the medium at the lower length scale is still continuous, whereas micromechanics based approaches may include local discontinuities due to the actual defects.

Selecting the appropriate damage variable(s) plays a key role within the framework of phenomenological continuum-damage models. Scalar damage variables are used to model isotropic, i.e., direction-independent, damaging behavior [16,23,24] and may be interpreted as the ratio of the effective load-bearing area to the total area. Due to its simplicity, scalar damage models are used frequently, also in recent publications [25–29]. To incorporate anisotropic damage into the continuum damage formulation, damage variables with higher tensor orders may be used, such as second-order damage variables [30–33] or fourth-order damage tensors [22, 32,34–37].

In continuum damage mechanics, selecting the damage variables is only half of the story: Care has to be taken when dealing with damage models that capture softening behavior of the material, as the material then favors localization [38] which cannot be captured on a volumetric mesh by standard local models. Rather, finite element computations lead to mesh-dependent predictions [39]. These observed “mesh dependencies” are actually just the ramifications of the underlying lack of mathematical sensibility of the softening damage model.

Different countermeasures were reported in the literature [40]. The simplest approach is based on viscous regularization [41–43], which implicitly enforces an upper bound on the damage increment for each mesh-element, thus limiting the dissipation and excluding the localization. Such strategies typically lead to reasonable models in practice, but lack a sound mathematical foundation.

Integral based approaches [44–47] incorporate long-range interactions by computing a filtered response of either the damage or the evaluated degradation function on a neighborhood of the material point. This averaging process smears out the intended localization and effectively excludes strong localization effects.

It is also possible to consider gradient-enhanced formulations [48–51], which add a gradient term of the damage variable within the damage evolution equation. From a physical point of view, the emergence of the damage gradient may be interpreted as quantifying the “average crack area”, and the additional gradient term permits to limit the energy dissipated when forming crack surfaces – the physical phenomenon responsible for the localization. Such approaches penalize strong fluctuations of damage in the same way as those strategies based on integral averages. In fact, most gradient-extended damage models may be equivalently expressed a non-local approaches by rewriting the evolution equation for the damage variable with a suitable Green’s function.

Despite their success, these reported ameliorations come with a number of shortcomings:

1. Incorporating non-local or gradient-enhanced damage models into existing software codes is often challenging. In particular, for commercial codes specific tricks are required. For instance, Navidtehrani et al. [52] report on an implementation of a phase field fracture model into the commercial software Abaqus hijacking the thermomechanical solver, i.e., the temperature is treated as the damage variable.
2. Both non-local and gradient-extended damage models require a length-scale parameter to be chosen. More often than not, the physical significance of this parameter is unclear and its identification based on experimental results is challenging. Also this length-scale parameter effectively excludes homogenization to apply [53]: If the length scale is proportional to the unit-cell size, it will become infinitesimal upon homogenization, removing the required regularization of the effective model to be sensible. In particular, no representative volume elements [54–56] emerge.

For these and other reasons, methods based on *convex relaxation* [57–60] were investigated recently. These works take a closer look at the mathematical underpinnings of the localization phenomena: In a variational setting, the considered damage models lack *quasi-convexity*. Morrey [61] identified the property of quasi-convexity as a necessary and sufficient condition for the existence of minimizers in the calculus of variations, provided certain necessary growth conditions on the integrands hold. Physically speaking,

quasi-convexity of an integrand means that a homogeneous variational problem with uniform boundary conditions admits a homogeneous solution. Interestingly, neither the shape of the considered body nor whether Dirichlet-, Neumann- or periodic boundary conditions are used plays a role to decide whether a specific integrand is quasi-convex or not, see Dacorogna [62]. For damage mechanics with softening, quasi-convexity of the integrands is not expected by physical considerations - cracks are supposed to form at a lower scale, leading to a non-homogeneous response. As quasi-convexity is a necessary condition for the existence of minimizers, it does not come as a surprise that softening behavior does in fact lead to ill-posed mathematical problems.

Methods based on convex relaxation intend to restore the quasi-convexity of the integrand by computing the (quasi-)convex envelope explicitly and to consider the obtained relaxed integrand as the ground truth. Such a strategy might be considered as adding "microstructural information", i.e., the heterogeneities obstructing quasi-convexity, into the picture. Thus, relaxation approaches operate in two stages: First, the model is selected. Secondly, the convex envelope is computed. Both stages involve *choices*. The real problem for the relaxation approach is actually *computing the envelope*, which amounts to solving a non-convex variational problem more or less explicitly. In this way, this difficulty of non-quasi-convexity is handled by an *analytical method*. Unfortunately, achieving this task is only possible in rare cases, and the choice of the original model and the type of convex envelope is driven by whether it can be handled analytically and explicitly or not. For instance, computing the quasi-convex envelope explicitly is notoriously difficult. Computing the convex envelope is typically simpler, and every convex function is also quasi-convex. Thus, the convex envelope is regularly considered although it is less physical than the quasi-convex envelope. Due to the convexification process, relaxation-based models are *local*, i.e., do not require non-local terms or damage-gradient terms for regularization. We wish to clarify that the term local model is used to distinguish such approaches from non-local damage models or gradient-enhanced formulations, which include neighborhood information to compute the material response at a single material point.

The described program was set up by Schwarz et al. [59] who considered an isotropic damage model without tension-compression asymmetry. To ensure coercivity of the functionals, a damage-rate limitation [63] was enforced. Then, the incremental condensed free energy was selected as the function to be convexified. Schwarz et al. [59] managed to solve the minimization problem with respect to the strain, but did not arrive at an explicit formula for the damage-minimization process. Rather, an approximation based on physical considerations - termed *emulated RVE* - was introduced and investigated.

1.2. Contributions

There are a number of advantages which make a convexified damage model attractive:

- The model is local, i.e., no filtered averages or damage-gradient terms are necessary.
- The material evaluation involves conventional internal variables only, is thermodynamically consistent and operates on material point level.
- The formulation does not involve internal length scale parameters, which may be challenging to calibrate experimentally.
- The implementation in standard commercial FE software, e.g., Abaqus, is straightforward via user material subroutines.
- The novel class of damage models is suitable for computational multiscale modeling frameworks due to its mesh-objective response and the absence of a length scale parameter. Thus, it may be directly embedded into FE^2 [64–66] or FE-FFT [67,68] codes.

However, there are two issues which must be taken care of. For a start, the model must be able to reproduce softening behavior. Otherwise, the damaging behavior observed in experiments cannot be reproduced accurately. Moreover, the (cross-)convex hull must be determined by some means [69–71]. Previous works used computationally convenient approximations: a pre-defined finite number of damageable phases [59] or an a-priori restriction to 1D with subsequent direction averaging [72,73].
The key contribution of the work at hand is that we compute the (cross-)convex envelope of the considered local damage models explicitly and analytically. In general, solving the latter problem is considered hard because it involves computing the absolute minimum of a non-convex variational problem. It appears therefore surprising that a closed-form solution could be found.

To be more precise, we compute the convex envelope of a rate-limited, non-convex standard scalar damage model in a time-discretized setting in Section 2, completing the conceptual agenda initiated by Schwarz et al. [59]. To do so, we impose a condition which is satisfied by a variety of reasonable damage models: The reciprocal function of the damage-degradation function should be convex. Under this condition, the regularization approach leads to a family of convex damage models.

As a central outcome of the convexification process, the damage models are formulated based on one-dimensional damage-distribution functions instead of a scalar damage variable, and the effective degradation computes as the harmonically averaged degradation function. Interestingly, the time evolution of the damage-distribution functions turns out to possess the structure of an optimal transport problem [74], which naturally emerges from the variational formulation of the convexified energy. Due to the structural analogy to optimal transport theory, we call the damage models *optimal transport* (OT) damage models.

We provide arguments for the existence of minimizers to the associated mechanical boundary value problems, which is essential for a reliable numerical approximation. The existence of a solution results from the convexity and the coercivity of the condensed incremental energy, see Section 3.3.

In Section 3, we derive the damage models for a constant time-step size explicitly. Additionally, we introduce an efficient numerical procedure to solve the constrained linear optimization problem using a one-dimensional Newton-type method. We also discuss the convexity properties of the incremental energy and the existence of continuous minimizers to the associated mechanical boundary-value problems. Section 3 also provides critical insights into the structure of the derived class of models: In contrast to traditional phenomenological continuum-damage models, which use damage variables of a specific tensor order as arguments, the emerging model involves a *damage-distribution function*. Moreover, this distribution enters the free energy via a harmonic average as a prefactor

to the Hookean undamaged free energy. This harmonic averages emerge naturally as a consequence of the convex relaxation process. From a continuum mechanical point of view, the appearance of both the damage distribution and the harmonic average does not come as a surprise: If we pursued a quasi-convexification, we would expect damage(d) microstructures to form. As we carry out a convexification process - which ignores kinematic compatibility of the strains and thus anisotropic spatial correlations - the harmonic mean emerges naturally as the dedicated homogenization operator in one spatial dimension of elastic rods connected in series. Alternatively, the harmonic average may also be considered as a realized Reuss bound on the effective stiffness. However, some care has to be taken, as we also obtain an evolution for the emerging damage distributions naturally. It is well known that the Hookean free energy gives rise to a convex function in terms of the strain and the compliance tensor [22]. As the compliance tensor of the convexified damage model is linear w.r.t. the damage distribution, the convexity of the model at hand is readily apparent, and the variety of advantages which comes with convexity is directly available.

In Section 4, we conduct computational investigations with respect to the novel class of scalar damage models, using methods of FFT-based computational micromechanics [75–77]. We start with computations on material point level, studying the influence of the damage model parameters and different damage-degradation functions. To take heterogeneous stress states into consideration, we first apply the damage model to the matrix material of composites with a single circular inclusion and subsequently to the matrix material of long fiber reinforced composites. The OT damage models lead to mesh-independent results even in the regime of softening, preventing localization. Thus, the models may be used to predict the mechanical behavior on continuum scale including materials with softening behavior in a reliable and efficient manner. In addition, the mesh-independence ensures that the OT damage model is applicable for homogenization problems as representative volume elements will emerge for increasing unit cell size.

1.3. Notation

We use a direct tensor notation or matrix-vector notation with an orthonormal basis $\{\boldsymbol{e}_1, \dots, \boldsymbol{e}_n\}$ in $n = 3$ dimension. We denote scalars with non-bold letters, e.g., b. Vectors are represented by non-cursive bold lowercase letters, e.g., $\mathbf{b}$, in matrix-vector notation and by cursive bold lowercase letters, e.g., $\boldsymbol{b}$, in the direct tensor notation. Bold cursive uppercase letters, e.g., $\boldsymbol{B}$, are used for tensors of second order and, e.g., $\mathbb{B}$, denote tensors of fourth order. For symmetric tensors of second order defined in a three-dimensional orthonormal basis, we use, e.g., $\boldsymbol{B} \hat{=} \mathtt{diag}(b_1, b_2, b_3)$, for the representation in the diagonalized form. The space of symmetric second-order tensors on $\mathbb{R}^n$ is represented by $\mathrm{Sym}(n)$. For simplicity, we introduce the following operations only for the direct tensor notation, but use the same notations also for operations in matrix-vector notation. The material time derivative of the scalar b is symbolized by $\dot{b}$. The linear mapping of a second-order tensor by a fourth order tensor is denoted by, e.g., $(\boldsymbol{A})_{ij} = (\mathbb{B}[\boldsymbol{C}])_{ij} = \boldsymbol{B}_{ijkl}\boldsymbol{C}_{kl}$.

2. Convex relaxation of a class of damage models

2.1. A rate-dependent damage model to be convexified

As our point of departure, we consider an isotropic scalar damage model [59] at small strains in an isothermal setting. We restrict to isotropic damage to keep the formulation as simple as possible to focus on the structure of the novel regularization technique and to avoid further complications. In general, a tensorial damage variable [37] could be used to model anisotropic damage processes. We use the framework of generalized standard materials (GSM) [78,79], and consider the free energy (density) as a function of the strain $\boldsymbol{\varepsilon}$ and the damage variable d

$$\psi : \mathrm{Sym}(n) \times [0, d_{\max}) \to \mathbb{R}_{\geq 0}, \quad \psi(\boldsymbol{\varepsilon}, d) = \frac{f(d)}{2}\, \boldsymbol{\varepsilon} \cdot \mathbb{C}[\boldsymbol{\varepsilon}], \tag{2.1}$$

where $\mathrm{Sym}(n)$ stands for the vector space of symmetric second-order tensors in $\mathbb{R}^n$ with $n = 2, 3$ spatial dimensions. The considered dissipation potential reads

$$\Psi : \mathbb{R} \to \mathbb{R}_{\geq 0} \cup \{+\infty\}, \quad \Psi(\dot{d}) = \begin{cases} r\,\dot{d}, & 0 \leq \dot{d} \leq \dot{d}_{\max}, \\ +\infty, & \text{otherwise.} \end{cases} \tag{2.2}$$

Here, $\dot{d}$ denotes the material time derivative of the internal variable d describing the damage, $d_{\max}$ refers to a positive number or plus infinity and determines the maximum attainable value of damage, $\mathbb{C}$ stands for an elastic stiffness tensor, corresponding to the undamaged state, and r is a positive dissipation parameter. Moreover, the phenomenological model involves a damage-degradation function

$$f : [0, d_{\max}) \to [0, 1], \tag{2.3}$$

which we assume to be continuous, strictly monotonically decreasing and to satisfy the "boundary conditions"

$$f(0) = 1 \quad \text{and} \quad \lim_{d \to d_{\max}} f(d) = 0. \tag{2.4}$$

For the work at hand, the following three mathematical equations are used for the degradation function, taken from the literature [3, 51,80]:

1. Exponential degradation:

$$f(d) = e^{-d}, \quad d \geq 0. \tag{2.5}$$

2. Linear degradation:

$$f(d) = 1 - d, \quad 0 \leq d \leq 1. \tag{2.6}$$

3. Quadratic degradation:

$$f(d) = (1 - d)^2, \quad 0 \leq d \leq 1. \tag{2.7}$$

As the damage degradation function modulates the remaining stiffness of the material, the stress-strain response of the damage model may be tailored to a specific material by selecting an adequate degradation function. Besides the three introduced functions (2.5)–(2.7), further options are available in literature, see for example Wu and Nguyen [81].

Last but not least, the model (2.1)-(2.2) involves a rate limitation $\dot{d}_{\max}$, which we assume positive and finite. Here, we follow the suggestion of Allix [63], who introduced the rate limitation $\dot{d}_{\max}$ to ensure the coercivity of the condensed energy, i.e., that the condensed energy tends to infinity as the norm of the strain tensor becomes arbitrarily large. If coercivity does not hold, minimizers might lie "at infinity", i.e., are trivial, and existence of minimizers for the model might fail [62]. We wish to stress that the rate limitation makes the model generally rate-dependent. Indeed, a generalized standard model is rate independent if and only if the dissipation potential (2.2) is positively homogeneous of degree one. Due to the damage rate limitation, the dissipation potential is not homogeneous and the damage model is rate-dependent.

In accordance with the setting of a GSM [78], the dissipation potential (2.2) is non-negative, lower semicontinuous as well as convex and fulfills the condition $\Psi(0) = 0$.

To ensure that the model is thermodynamically consistent, we take the Clausius-Duhem inequality (CDI) [82, Chapter 13] for an isothermal model approach

$$0 \overset{!}{\leq} \boldsymbol{\sigma} \cdot \dot{\boldsymbol{\varepsilon}} - \dot{\psi}(\boldsymbol{\varepsilon}, d) \equiv \left[\boldsymbol{\sigma} - \frac{\partial \psi}{\partial \boldsymbol{\varepsilon}}(\boldsymbol{\varepsilon}, d)\right] \cdot \dot{\boldsymbol{\varepsilon}} - \frac{\partial \psi}{\partial d} \cdot \dot{d} \tag{2.8}$$

into account, which has to hold for all strain rates and damage rates. Derived from the CDI (2.8), the associated stress computes as

$$\boldsymbol{\sigma} \equiv \frac{\partial \psi}{\partial \boldsymbol{\varepsilon}}(\boldsymbol{\varepsilon}, d) = f(d)\, \mathbb{C}[\boldsymbol{\varepsilon}], \tag{2.9}$$

for the model at hand, i.e., the undamaged stiffness $\mathbb{C}$ is uniformly weakened via the degradation function (2.3). To satisfy the non-negativity of the second term of the CDI, we assume the damage evolution to be governed by Biot's equation [83]

$$-\frac{\partial \psi}{\partial d}(\boldsymbol{\varepsilon}, d) \in \partial \Psi\big(\dot{d}\big) \tag{2.10}$$

for a prescribed strain path and a given initial condition for the damage variable, where $\partial\Psi$ stands for the subdifferential [84] of the (convex) dissipation potential (2.2) and the quantity $-\partial\psi(\boldsymbol{\varepsilon}, d)/\partial d$ is called *driving force*.

We consider an implicit Euler discretization in time, i.e., a sequence $t_0, t_1, \ldots$ of increasing time steps and wish to determine solutions to the time-discrete equivalent of Biot's Eq. (2.10)

$$-\frac{\partial \psi}{\partial d}(\boldsymbol{\varepsilon}, d) \in \partial \Psi\left(\frac{d - d^k}{\Delta t_k}\right) \quad \text{with} \quad \Delta t_k = t_{k+1} - t_k, \tag{2.11}$$

where we write $d \equiv d^{k+1}$ for simplicity and assume the previous value d^k to be known. The condition (2.11) characterizes critical points of the optimization problem [85,86]

$$\psi(\boldsymbol{\varepsilon}, d) + \Delta t_k\, \Psi\left(\frac{d - d^k}{\Delta t_k}\right) \longrightarrow \min_{d \in [0, d_{\max})}, \tag{2.12}$$

where the minimum of the function is called *condensed incremental energy* [86]

$$\psi_{\text{cond}}(\boldsymbol{\varepsilon}) = \min_{d \in [0, d_{\max})} \psi(\boldsymbol{\varepsilon}, d) + \Delta t_k\, \Psi\left(\frac{d - d^k}{\Delta t_k}\right), \quad \boldsymbol{\varepsilon} \in \text{Sym}(n). \tag{2.13}$$

Considering the model at hand, the optimization problem (2.12) takes the form

$$\frac{f(d)}{2}\, \boldsymbol{\varepsilon} \cdot \mathbb{C}[\boldsymbol{\varepsilon}] + \mathcal{D}\big(d^k, d\big) \longrightarrow \min_{0 \leq d - d^k \leq \Delta t_k\, \dot{d}_{\max}} \tag{2.14}$$

with the *dissipation distance*

$$\mathcal{D}\big(d^k, d\big) = r\,(d - d^k), \tag{2.15}$$

which may be understood as the energy dissipated during the damage progression from the damage state d^k to d. For the degradation functions (2.5)–(2.7), the discrete evolution of the damage variable d may be determined analytically. For instance, the exponential degradation function (2.5) leads to the prescription

$$d = \min\left(\max\left(d^k, \ln \frac{\psi_0(\boldsymbol{\varepsilon})}{r}\right), d^k + \Delta t_k\, \dot{d}_{\max}\right) \tag{2.16}$$

with the undamaged elastic energy

$$\psi_0 : \text{Sym}(n) \to \mathbb{R}_{\geq 0}, \quad \psi_0(\boldsymbol{\varepsilon}) = \frac{1}{2}\boldsymbol{\varepsilon} \cdot \mathbb{C}[\boldsymbol{\varepsilon}]. \tag{2.17}$$

For the quadratic degradation (2.7), one computes

$$d = \min\left(\max\left(d^k, 1 - \frac{r}{2\,\psi_0(\boldsymbol{\varepsilon})}\right), d^k + \Delta t_k\,\dot{d}_{\max}\right), \tag{2.18}$$

whereas the linear degradation function (2.6) yields the result

$$d = \begin{cases} d^k, & \psi_0(\boldsymbol{\varepsilon}) < r, \\ d^k < d < d^k + \Delta t_k\,\dot{d}_{\max}, & \psi_0(\boldsymbol{\varepsilon}) = r, \\ d^k + \Delta t_k\,\dot{d}_{\max}, & \psi_0(\boldsymbol{\varepsilon}) > r. \end{cases} \tag{2.19}$$

As the linear degradation function leads to a driving force which is independent of the damage variable

$$-\frac{\partial \psi}{\partial d}(\boldsymbol{\varepsilon}, d) = \psi_0(\boldsymbol{\varepsilon}), \tag{2.20}$$

the damage evolution equation is ill-posed, resulting in an indeterminate damage state if the undamaged elastic energy exactly equals the damage parameter r, see Eq. (2.19). However, in our numerical simulations this case did not occur. For a finite-strain setting without damage-rate limitation, Melchior et al. [73, Section 2.4] reported a similar phenomenon due to the applied linear degradation function, where a phase of the material tends to the maximal energetically possible damage evolution.

Let us consider an undamaged material with $d^0 = 0$ and compute the minimum value of the undamaged elastic energy $\psi_0(\boldsymbol{\varepsilon})$ which is required for damage onset. For both the exponential and the linear degradation function, the undamaged elastic energy needs to satisfy the equation

$$\psi_0(\boldsymbol{\varepsilon}) = r, \tag{2.21}$$

whereas the required undamaged elastic energy equals

$$\psi_0(\boldsymbol{\varepsilon}) = r/2 \tag{2.22}$$

for the quadratic degradation function. Hence, we observe that the model parameter r limits the elastic range, i.e., it determines the onset of inelastic deformation. According to Eqs. (2.21) and (2.22), the quadratic degradation function leads to an earlier onset of damage compared to the other two degradation functions when selecting the same value for the parameter r. In case that all three degradation functions are requested to start the damage evolution at an equal level of undamaged elastic energy, the parameter r needs to be selected twice as high for the quadratic degradation function.

Although these models lead to sensible results on a material-point level – thanks to the rate limitation (2.2) – producing a well-defined evolution on the continuum scale, when used as a constitutive model for a component, for instance, is more challenging. Under suitable growth conditions on the integrand, a celebrated result of Morrey [61] states that a necessary and sufficient condition for the existence of minimizers to the variational problem involving such an integrand is the quasi-convexity of the integrand. Whether the condensed incremental energy of the considered damage model is quasi-convex or not is not known to the authors. Presumably, it is not.

A possible way to construct a well-posed evolution is to compute a suitable quasi-convex envelope of the condensed incremental energy. Unfortunately, we are neither aware of an explicit analytical solution for this problem nor an efficient computational scheme, despite recent progress [60,87]. Therefore, we follow the route sketched by Schwarz and coworkers [59]: We compute the convex envelope of the condensed incremental energy. Every convex function is also quasi-convex [88], so the incremental problems will be amenable to Morrey's existence result. The price to pay is that the model becomes less physically interpretable and that the models we started out with may be significantly altered by the convexification process. Fortunately, computational experiments will permit us to gain insight into the differences which are created and show that the alteration is small for the considered material and load cases, see Section 3.

2.2. The convex envelope

The purpose of this section is to compute the convex envelope for the damage model (2.1)-(2.2) under natural conditions on the damage-degradation function (2.3).

Suppose that a specific function

$$F : \mathbb{R}^m \to \mathbb{R} \tag{2.23}$$

is given. Then, the convex envelope F^c is defined as the largest convex function whose graph is point-wise less or equal than the graph of the given function F. Geometrically, the epigraph of the convex envelope F^c corresponds to the convex hull of the epigraph of the function F, see Fig. 1. Thus, the following explicit characterization

$$F^c(\bar{\boldsymbol{x}}) = \min\left\{ \sum_{i=0}^{m} c_i\,F(\boldsymbol{x}_i) \,\middle|\, \boldsymbol{x}_i \in \mathbb{R}^m,\ c_i \geq 0 \text{ for } i = 0, 1, \dots, m,\ \sum_{i=0}^{m} c_i = 1 \text{ and } \sum_{i=0}^{m} c_i\,\boldsymbol{x}_i = \bar{\boldsymbol{x}} \right\} \tag{2.24}$$

of the convex envelope F^c for $\bar{\boldsymbol{x}} \in \mathbb{R}^m$ emerges. Thus, for any point $\bar{\boldsymbol{x}} \in \mathbb{R}^m$, one considers all convex combinations

$$\bar{\boldsymbol{x}} = \sum_{i=0}^{m} c_i\,\boldsymbol{x}_i \tag{2.25}$$

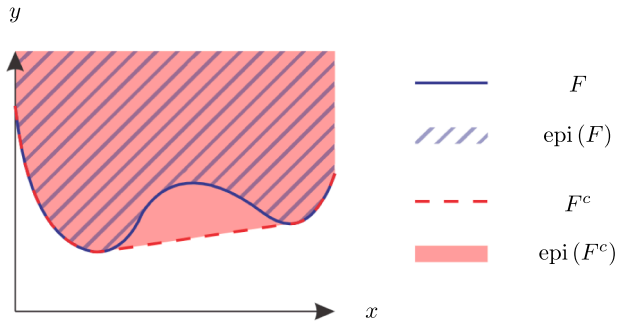

Fig. 1. Illustration of a one-dimensional non-convex function F, its convex envelope F^c and the epigraphs of both functions epi(F) and epi(F^c).

of the point $\bar{\boldsymbol{x}}$, where $m+1$ terms are sufficient in m dimensions to represent a general convex combination by Caratheodory's Theorem [89], and seeks the smallest convex combination of the corresponding objective values.
For the problem (2.1)-(2.2) at hand, we start with the first time step with index $k=0$ and consider the condensed incremental energy

$$\psi_{\text{cond}}(\bar{\boldsymbol{\varepsilon}}) = \min \left\{ \frac{f(d)}{2}\, \bar{\boldsymbol{\varepsilon}} \cdot \mathbb{C}[\bar{\boldsymbol{\varepsilon}}] + r\left(d - d^0\right) \,\middle|\, 0 \le d - d^0 \le \Delta t_0\, \dot{d}_{\max} \right\}, \quad \bar{\boldsymbol{\varepsilon}} \in \text{Sym}(n), \tag{2.26}$$

for $m = n(n+1)/2$ dimensions. Thus, the convex envelope (2.24) of the condensed incremental energy (2.26) becomes

$$\psi^c_{\text{cond}}(\bar{\boldsymbol{\varepsilon}}) = \min \left\{ \sum_{i=0}^{m} c_i \left(\frac{f\left(d_i\right)}{2}\, \boldsymbol{\varepsilon}_i \cdot \mathbb{C}_i\left[\boldsymbol{\varepsilon}_i\right] + r\left(d_i - d^0\right) \right) \,\middle|\, \sum_{i=0}^{m} c_i\, \boldsymbol{\varepsilon}_i = \bar{\boldsymbol{\varepsilon}}, \quad 0 \le d_i - d^0 \le \Delta t_0\, \dot{d}_{\max} \right\} \tag{2.27}$$

for $m = n(n+1)/2$, $\bar{\boldsymbol{\varepsilon}} \in \text{Sym}(n)$ and weighting coefficients c_i which satisfy the simplex constraint (2.24).
Thus, we observe that the "mixing" which is intrinsic to computing a convex envelope (2.24) also entails a "mixing" of internal variables in the sense of creating a "microstructure". Indeed, instead of a *single value* of the internal variable d, up to $n(n+1)/2+1$ internal variables may appear in the first load step due to the convexification. For the second load step, each of the internal variables may decompose further - leading to a process of more and more internal variables for the subsequent time steps. Put differently, a $(n(n+1)/2+1)$-ary tree whose depth corresponds to the number of time steps is created.
To avoid these technicalities, it is actually more convenient to work with a continuum than with a possibly large number of discrete variables. More precisely, returning to the abstract setting (2.23) for clarity, we consider fields

$$\boldsymbol{x} : [0,1] \to \mathbb{R}^m \tag{2.28}$$

on the unit interval. This domain has no intrinsic physical meaning, but permits us to express the convex envelope (2.24) in the form

$$F^c(\bar{\boldsymbol{x}}) = \min \left\{ \langle F(\boldsymbol{x}) \rangle_{[0,1]} \,\middle|\, \boldsymbol{x} : [0,1] \to \mathbb{R}^m, \quad \langle \boldsymbol{x} \rangle_{[0,1]} = \bar{\boldsymbol{x}} \right\} \tag{2.29}$$

for a prescribed vector $\bar{\boldsymbol{x}} \in \mathbb{R}^m$, where the symbol

$$\langle q \rangle_{[0,1]} = \int_0^1 q(s)\, \mathrm{d}s \tag{2.30}$$

encodes the mean of a function q on the unit interval $[0,1]$. The equivalence of the two expressions (2.24) and (2.29) is readily seen.
The right-hand side in Eq. (2.29) is certainly not larger than the right-hand side in Eq. (2.24), as one may define the piece-wise constant function

$$\boldsymbol{x} : [0,1] \to \mathbb{R}^m, \quad \boldsymbol{x}(s) = \boldsymbol{x}_i \text{ if } \sum_{j=0}^{i} c_i \le s < \sum_{j=0}^{i+1} c_i \quad \text{for} \quad i = 0, 1, \dots, m-1. \tag{2.31}$$

On the other hand, the right-hand side in Eq. (2.24) is certainly not larger than the right-hand side in Eq. (2.29), as any continuous convex combination

$$\bar{\boldsymbol{x}} = \langle \boldsymbol{x} \rangle_{[0,1]} \tag{2.32}$$

may be represented by a finite convex combination

$$\bar{\boldsymbol{x}} = \sum_{i=0}^{m} c_i\, \boldsymbol{x}_i, \quad \boldsymbol{x}_i \in \mathbb{R}^m, \quad c_i \ge 0, \quad \sum_{i=0}^{m} c_i = 1, \tag{2.33}$$

with no more than $m+1$ terms as a consequence of Caratheodory's Theorem [89].
Returning to the problem (2.27) at hand, we thus consider the following convex envelope

$$\psi^c_{\text{cond}}(\bar{\boldsymbol{\varepsilon}}) = \min \left\{ \left\langle \frac{f(d)}{2}\, \boldsymbol{\varepsilon} \cdot \mathbb{C}[\boldsymbol{\varepsilon}] + r(d - d^-) \right\rangle_{[0,1]} \,\middle|\, \langle \boldsymbol{\varepsilon} \rangle_{[0,1]} = \bar{\boldsymbol{\varepsilon}}, \quad d^- \le d \le d^+ \right\} \tag{2.34}$$

Here, $d^{\pm} : [0,1] \to [d, d_{\max})$ are piece-wise constant functions. For the first load step, we have $d^- \equiv d^0$ and $d^+ = d^0 + \Delta t_0\, \dot{d}_{\max}$. The introduction of the fields d^- and d^+ permits to treat subsequent time steps in a uniform fashion.

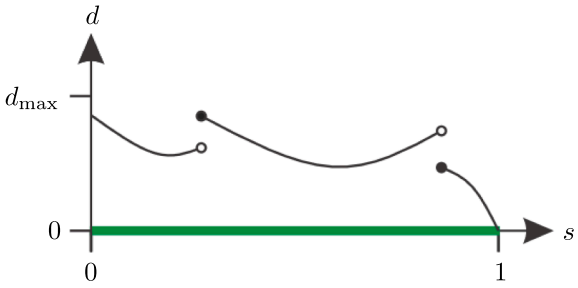

Fig. 2. Rod with local damage variable d.

$$\bar{E} = \left(\sum_{i=1}^{4} \frac{\ell_i}{E_i} \right)^{-1}, \quad \sum_{i=1}^{4} \ell_i = 1$$

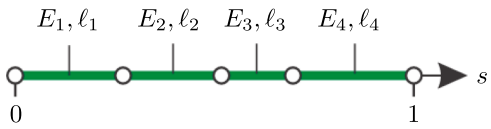

Fig. 3. Elastic rods connected in series with elastic moduli E_i, lengths ℓ_i and cross-sectional area $A_i = A$.

2.3. Computing the convex envelope explicitly

The goal of this section is to compute the convex envelope (2.34)

$$\psi^c_{\text{cond}}(\bar{\varepsilon}) = \min \left\{ \left\langle \frac{f(d)}{2}\, \varepsilon \cdot \mathbb{C}[\varepsilon] + r\,(d - d^-) \right\rangle_{[0,1]} \,\middle|\, \langle \varepsilon \rangle_{[0,1]} = \bar{\varepsilon}, \quad d^- \le d \le d^+ \right\} \tag{2.35}$$

for a prescribed strain $\bar{\varepsilon} \in \text{Sym}(n)$ and given piece-wise constant functions $d^{\pm} : [0,1] \to [d, d_{\max})$ which we assume to satisfy the inequality $d^- \le d^+$ point-wise. Physically speaking, the problem (2.35) may be imagined as a single initially elastic rod which undergoes damage. The domain $[0,1]$ represents the "material points" of the rod, and the stiffness at each material point is degraded by the local damage variable $d(s)$ at the location $s \in [0,1]$, see Fig. 2. The mental image of the rod makes sense because the strains appearing in the problem (2.35) do not account for kinematic compatibility as a result for considering the *convex* envelope, and not the quasi-convex one.

As a first step, Schwarz et al. [59] observed the identity

$$\min_{\langle \varepsilon \rangle_{[0,1]} = \bar{\varepsilon}} \left\langle \frac{f(d)}{2}\, \varepsilon \cdot \mathbb{C}[\varepsilon] \right\rangle_{[0,1]} = \frac{\bar{f}(d)}{2}\, \bar{\varepsilon} \cdot \mathbb{C}[\bar{\varepsilon}] \tag{2.36}$$

with the harmonically averaged degradation function

$$\bar{f}(d) = \left\langle f(d)^{-1} \right\rangle^{-1}_{[0,1]}. \tag{2.37}$$

For the convenience of the reader, the mathematical arguments are collected in Appendix A. From a homogenization point-of-view in one spatial dimension, the harmonic average (2.39) emerges naturally as the homogenization operator of elastic rods connected in series [90], illustrated in Fig. 3. With this insight at hand, we are left to evaluate the minimization problem

$$\bar{f}(d)\, \psi_0(\bar{\varepsilon}) + r\, \langle d - d^- \rangle_{[0,1]} \longrightarrow \min_{d^- \le d \le d^+} \tag{2.38}$$

with the elastic energy ψ_0 of the undamaged state (2.17). To proceed beyond the state of the art [59], we need to make an additional assumption.

We require that the function

$$g : [d, d_{\max}) \to [0, \infty), \quad g(d) = \frac{1}{f(d)}, \tag{2.39}$$

is well-defined and **convex**. This assumption is readily seen to hold for the three specific cases (2.5)–(2.7) of damage-degradation functions which we have in mind. For the exponential degradation function (2.5), the function g takes the form $g(d) = e^d$, which is clearly a convex function. For the linear and the quadratic degradation functions, the reciprocal function (2.39) takes the form $g(d) = (1-d)^{-m}$ for $m = 1$ and $m = 2$. This function is convex on the interval $[0,1)$, as can be read off the second derivative

$$g''(d) = m\,(m+1)\, \frac{1}{(1-d)^{m+2}}, \tag{2.40}$$

which turns out to be positive for $d \in [0,1)$.
Under the convexity assumption on the function (2.39), the following alternative expression

$$\psi^c_{\text{cond}}(\bar{\varepsilon}) = \min_{\phi:[0,1]\to[0,1]} \left\langle (1-\phi) f(d^-)^{-1} + \phi\, f\big(d^+\big)^{-1} \right\rangle^{-1}_{[0,1]} \psi_0(\bar{\varepsilon}) + r \left\langle \phi\big(d^+ - d^-\big) \right\rangle_{[0,1]} \tag{2.41}$$

is valid. The derivation of this result comprises Appendix B. In fact, when preparing the revised manuscript we discovered that Francfort and co-workers [91,92] provided a result that is equivalent to the expression (2.41) for the linear degradation function (2.6) and the first time step.
Let us discuss the ramifications of the formula (2.41). The result (2.41) may be understood readily via the previously introduced analogy with an elastic rod whose stiffness is heterogeneous along the rod. At every continuum point of the rod with Young's modulus $E(d^-)$, there is a maximum damage to be attained during this time step, which would lead to the Young's modulus $E(d^+)$ (during unloading), which is lower than $E(d^-)$. The model (2.41) predicts that either the continuum point remains undamaged or is damaged as much as possible. The "volume fraction" ϕ in Eq. (2.41) indicates the fraction of such continuum points which damage fully, and the remaining $1-\phi$ fraction of continuum points remain unscathed.
To be more explicit, we study the first time step, where the bounding functions $d^\pm$ are actually constant with values

$$d^- = d^0 \quad \text{and} \quad d^+ = d^0 + \Delta t_0\, \dot{d}_{\max}. \tag{2.42}$$

Then, the optimization problem (2.41) takes the form

$$\psi^c_{\text{cond}}(\bar{\varepsilon}) = \min_{\phi_0\in[0,1]} \left[\Big((1-\phi_0) f\big(d^0\big)^{-1} + \phi_0\, f\big(d^0 + \Delta t_0\, \dot{d}_{\max}\big)^{-1} \Big)^{-1} \psi_0(\bar{\varepsilon}) + r\, \phi_0\, \Delta t_0\, \dot{d}_{\max} \right] \tag{2.43}$$

with $\phi_0 = \langle \phi \rangle_{[0,1]}$. Thus, we observe that intermediate damage states in the interior of the interval $[d^0, d^0 + \Delta t_0\, \dot{d}_{\max}]$ are not attained. Rather, a mixing of the extreme states, i.e., the end points of the interval, with mixing coefficients $1-\phi_0$ and ϕ_0 occur. In the mental rod model, a fraction of ϕ_0 of continuum points within the rod are damaged as much as possible, and the remaining $1-\phi_0$ points remain in their virgin state. Here, the role of the damage-rate limitation $\dot{d}_{\max}$ becomes apparent: The model (2.43) predicts that certain points damage as much as possible. If there was no limitation to the damage increment, the specimen would fail instantly, leading to *complete damage* and recovering the ill-posed damage-evolution problem we started out with.
Subsequent time steps also follow such a mixing, triggering a further splitting of the attainable states, leading to *damage distributions*. In case the time increment is constant, an explicit expression of the resulting damage model can be constructed, see Section 3.1. Whereas the damage model is rate-dependent, in general, for the specific case with unlimited damage rate $\dot{d} \to \infty$, the damage model becomes rate-independent. In addition, the damage model may remain rate-independent, even for finite damage rate limitations, in case the actual damage increments are smaller than the maximum admissible damage increments, i.e., the damage rate limitation is inactive.
The model formulation in Eq. (2.41) only includes the macroscopic strain $\bar{\varepsilon}$ explicitly, and the distinction between the microscopic strains ε_i and the macroscopic strain $\bar{\varepsilon}$ is not required anymore. Thus, we omit the bar over the macroscopic strain throughout the remaining manuscript for simplicity, i.e., the notation ε is used for the macroscopic strain.

2.4. The optimal transport point-of-view

The transition from discrete attained states (2.24) to a continuum description (2.29) turned out to be beneficial for the mathematical treatment of the convex relaxation problem. Indeed, we could reduce the technicalities and arrive at a unified description of the emerging constitutive model which is valid for all time steps. Despite these advantages of the continuum description in terms of damage *fields*, there are some downsides, in particular in terms of the uniqueness and interpretation of the results. More precisely, as we consider a convex envelope, and not a quasi-convex one, there is no natural spatial "order" on the attained damage values. In particular, for a given damage state realizing the minimum (2.35), we may re-order this state in an arbitrary way and obtain another optimal damage state. This circumstance is a direct consequence of the lacking spatial correlation of th convex envelope.
Thus, one observes that the spatial arrangement of the damage values is not relevant. However, the *distribution* of the damage values turns out to be the expressive value of significance. In mathematical terms, instead of a field

$$d : [0,1] \to [0, d_{\max}), \tag{2.44}$$

we consider the probability measure μ on the set $[0, d_{\max})$ of attainable damage values. In particular, for a continuous function $\Phi : [0, d_{\max}) \to \mathbb{R}$, we notice the equality

$$\int_0^1 \Phi(d(s))\, \mathrm{d}s = \int_0^{d_{\max}} \Phi(d)\, \mathrm{d}\mu(d), \tag{2.45}$$

where the letter d on the left-hand side stands for the damage field d, whereas the right-hand side involves the letter d as the variable of integration. The Eq. (2.45) may be interpreted as some form of the co-area formula.
In view of the Eq. (2.45), the relevant integral quantities of the field d may be expressed equivalently via statistics of the associated probability measure μ. Moreover, under a re-ordering of the domain $[0,1]$, the probability measure μ remains unaltered.
These observations motivate us to consider the probability measure μ as the primary quantity of interest describing the phase space

of the relaxed damage model. In fact, we may express the free energy (2.1) in the form

$$\psi(\varepsilon,\mu)=\left(\int_0^{d_{\max}} f(d)^{-1}\,\mathrm{d}\mu(d)\right)^{-1}\psi_0(\varepsilon), \tag{2.46}$$

where we abuse notation and retain the letter ψ for the free energy, although it has been reserved for damage *functions* previously. With respect to the framework of a GSM, the time derivative of the free energy with respect to the evolution of the probability measure μ follows as

$$\frac{\partial\psi}{\partial\mu}(\varepsilon,\mu)\,\dot{\mu}=-\frac{\displaystyle\int_0^{d_{\max}} f(d)^{-1}\,\mathrm{d}\dot{\mu}(d)}{\left(\displaystyle\int_0^{d_{\max}} f(d)^{-1}\,\mathrm{d}\mu(d)\right)^2}\psi_0(\varepsilon), \tag{2.47}$$

implicitly defining the thermodynamical driving force.

For a fixed time step k, the transition from the previous measure μ^k to the current measure μ involves optimal transportation [69–71,74,93]. In this context, a *transportation plan* between the probability measures μ^k and μ is a measure π on the product space $[0,d_{\max})\times[0,d_{\max})\equiv[0,d_{\max})^2$ which satisfies the push-forward conditions

$$\left(\mathrm{pr}_1\right)_*\pi=\mu^k\quad\text{and}\quad\left(\mathrm{pr}_2\right)_*\pi=\mu \tag{2.48}$$

in terms of the projections $\mathrm{pr}_i(d_1,d_2)=d_i$ $(i=1,2)$. The conditions (2.48) state that the transportation plan π distributes the mass from the measure μ^k to the measure μ. An equivalent formulation of the conditions (2.48) is that for any continuous function $\Phi:[0,d_{\max})\to\mathbb{R}$ and any bounded interval I, the conditions

$$\int_{I\times[0,d_{\max})}\Phi(d_1)\,\mathrm{d}\pi(d_1,d_2)=\int_I\Phi(d_1)\,\mathrm{d}\mu^k(d_1)\quad\text{and}\quad\int_{[0,d_{\max})\times I}\Phi(d_2)\,\mathrm{d}\pi(d_1,d_2)=\int_I\Phi(d_2)\,\mathrm{d}\mu^k(d_2) \tag{2.49}$$

must hold true. With the notation of transportation plan at hand, we may describe the transition from the previous state μ^k to the current state μ mathematically. More precisely, the probability measure μ minimizes the functional

$$\left(\int_0^{d_{\max}} f(d)^{-1}\,\mathrm{d}\mu(d)\right)^{-1}\psi_0(\varepsilon)+\mathcal{D}(\mu^k,\mu), \tag{2.50}$$

where the dissipation distance $\mathcal{D}(\mu^k,\mu)$ is the minimum of the Monge-Kantorovich problem [94]

$$\mathcal{D}(\mu^k,\mu)=\min\left\{\int_{[0,d_{\max})^2}\kappa(d_1,d_2)\,\mathrm{d}\pi(d_1,d_2)\,\middle|\,\pi\text{ is a transportation plan from }\mu^k\text{ to }\mu\right\}, \tag{2.51}$$

formulated in terms of the cost function

$$\kappa(d_1,d_2)=\begin{cases} r(d_2-d_1), & d_1\le d_2\le d_1+\Delta t_k\,\dot{d}_{\max},\\ +\infty, & \text{otherwise.}\end{cases} \tag{2.52}$$

The formulation (2.50) highlights the convexity of the considered model. Indeed, the traditional Hookean free energy

$$\psi^{\mathrm{Hooke}}(\varepsilon,\mathbb{S})=\frac{1}{2}\varepsilon\cdot\mathbb{S}^{-1}[\varepsilon], \tag{2.53}$$

formulated in terms of the strain ε and the compliance tensor $\mathbb{S}$, turns out to be a convex function of both arguments, see Görthofer et al. [22]. In particular, the free energy (2.46) is also a convex function of its arguments ε and μ. First, the undamaged elastic energy $\psi_0(\varepsilon)$ is convex in its argument ε. Secondly, the harmonic mean of the function $f(d)$ is also convex in the argument μ, essentially as the integration against a probability measure is a linear operation and the reciprocal function is convex for positive input values. As the minimum value of a Monge-Kantorovich problem is a convex function of the marginals μ^k and μ [74,93], the dissipation distance (2.51) is convex in the argument μ too. Thus, the incremental minimization problem (2.50) is a convex optimization problem, as well. As a result, the condensed incremental energy

$$\psi_{\mathrm{cond}}(\varepsilon)=\min\left\{\left(\int_0^{d_{\max}} f(d)^{-1}\,\mathrm{d}\mu(d)\right)^{-1}\psi_0(\varepsilon)+\mathcal{D}(\mu^k,\mu)\,\middle|\,\mu\text{ is a probability measure on }[0,d_{\max})\right\} \tag{2.54}$$

turns out to be a convex function.

We wish to close this excursion to the world of mathematical optimal transport with an interpretation of the results discussed in Section 2.4. Under the convexity assumption (2.39) on the reciprocal of the damage-degradation function, the solution μ of the optimization problem (2.50) will be a sum of Dirac measures, provided the previous internal variable μ^k was a sum of Dirac measures, as well. In particular, if the first time step involves a fully intact material, i.e.,

$$\mu^0=\delta_0, \tag{2.55}$$

where δ_d stands for the Dirac measure on the set $[0,d_{\max})$ concentrated at the damage value d, the first time step will lead to a damage distribution

$$\mu^1=(1-\phi)\,\delta_0+\phi\,\delta_{\Delta t_0\,\dot{d}_{\max}}\quad\text{for some}\quad\phi\in[0,1]. \tag{2.56}$$

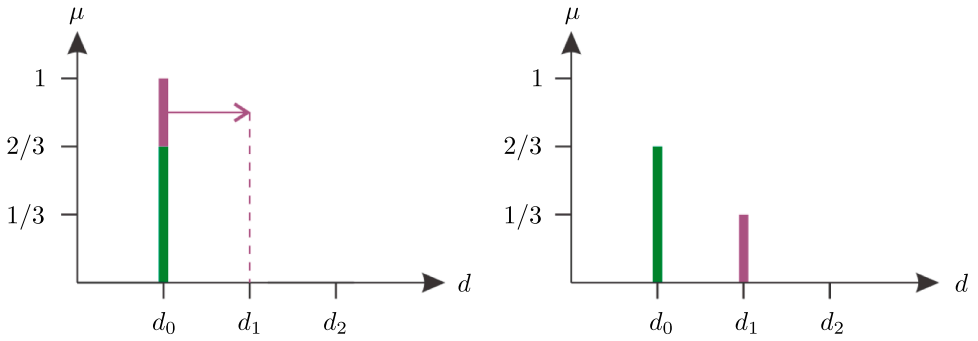

(a) First time step with $\mu^0 = \delta_{d_0}$ and $\mu^1 = \frac{2}{3}\delta_{d_0} + \frac{1}{3}\delta_{d_1}$

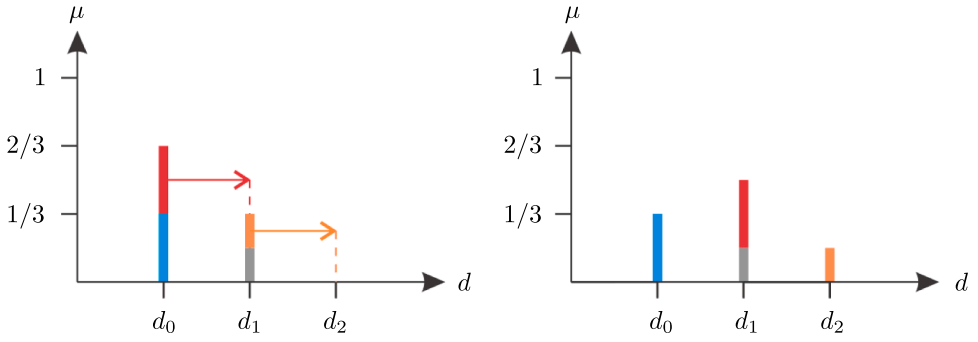

(b) Second time step with $\mu^1 = \frac{2}{3}\delta_{d_0} + \frac{1}{3}\delta_{d_1}$ and $\mu^2 = \frac{1}{3}\delta_{d_0} + \frac{1}{2}\delta_{d_1} + \frac{1}{6}\delta_{d_2}$

Fig. 4. Evolution of a discrete damage distribution with three damage values for two time steps.

Suppose the kth time step is described by the discrete measure

$$\mu^k = \sum_{j=1}^{N} \rho_j \, \delta_{d_j}, \quad \rho_j \geq 0, \quad \sum_{j=1}^{N} \rho_j = 1, \tag{2.57}$$

and distinct damage values $d_j \in [0, d_{\max})$, the subsequent time step will have the form

$$\mu^k = \sum_{j=1}^{N} \rho_j \left[(1 - \phi_j)\delta_{d_j} + \phi_j \delta_{d_j + \Delta t_k \, \dot{d}_{\max}} \right] \tag{2.58}$$

with suitable "fractions" $\phi_j \in [0, 1]$. Due to the connection of the convexified damage model with the theory of optimal transport, we call it *optimal transport* (OT) damage model.

In Fig. 4, the evolution of a discrete damage distribution with the three damage values d_i $(i = 0, 1, 2)$ is shown for two time steps. The initial discrete damage distribution is described by the measure $\mu^0 = \delta_{d_0}$, i.e., the damage fractions are $\rho_0^0 = 1$ and $\rho_1^0 = \rho_2^0 = 0$. During the first time step, see Fig. 4(a), damage mass is transferred from the damage value d_0 to the damage value d_1 with the transition fraction $\phi_0^0 = 1/3$. The damage distribution at the end of the first time step is $\mu^1 = 2/3\,\delta_{d_0} + 1/3\,\delta_{d_1}$. In the second time step, see Fig. 4(b), the evolution of the damage distribution is characterized by a damage transportation from the damage value d_0 to the damage value d_1 as well as a damage transportation from the damage value d_1 to the damage value d_2, both with the transition fraction $\phi_0^1 = \phi_1^1 = 1/2$. The updated damage distribution reads $\mu^2 = 1/3\,\delta_{d_0} + 1/2\,\delta_{d_1} + 1/6\,\delta_{d_2}$.

The section at hand is mostly informative, i.e., it puts the results on the convex envelope (2.41) into perspective. Such a formulation appears to be imperative if we were interested in recovering a limit for vanishing time steps $\Delta t_i \to 0$, i.e., a time-continuous model. Indeed, we started out with a time-continuous model (2.23)-(2.24), and performed a convex relaxation at a time-discrete level. The resulting model may be treated numerically - and we will provide details in Section 3. However, from a continuum mechanical point of view, it is desirable to recover a time-continuous description, as well. We shall not do so here explicitly. Rather, we remark that the mathematical theory of optimal transport is the natural framework for such a task: The time-continuous model naturally involves probability measures as internal variables. These measures encode a *damage distribution* in a natural way. The latter insight might provide a reasonable continuum-mechanical interpretation of the convex relaxation process.

3. Computational mechanics of the damage model

3.1. Discussion of the model

In this section, we work out the mechanical aspects of the continuum-damage model resulting from the relaxation procedure (2.41) under the assumption that the time-step size $\Delta t_k \equiv \Delta t$ is constant. In particular, assuming initial damage of zero, the attainable damage states of the model are given by the sequence

$$0, \Delta t\, \dot{d}_{\max}, 2\,\Delta t\, \dot{d}_{\max}, 3\,\Delta t\, \dot{d}_{\max}, \dots \tag{3.1}$$

As we are considering a finite number of time steps, and we also enforce a maximum damage value $d_{\max}$, it is sufficient to restrict to a finite number

$$d_0, d_1, \dots, d_N \tag{3.2}$$

or *ordered* damage states

$$d_j = \min\left(j\,\Delta t\, \dot{d}_{\max}, d_{\max}\right), \quad j = 0, 1, \dots, N, \tag{3.3}$$

i.e., which satisfy the inequalities

$$d_j < d_{j+1} \quad \text{for} \quad j = 0, 1, \dots, N-1. \tag{3.4}$$

The phase-space of the internal variables comprises all damage fractions

$$\boldsymbol{\rho} \equiv \begin{bmatrix} \rho_0 & \cdots & \rho_N \end{bmatrix}^{\mathsf{T}} \tag{3.5}$$

which satisfy the simplex constraints

$$\rho_j \geq 0 \quad (j = 0, 1, \dots, N) \quad \text{and} \quad \sum_{j=0}^{N} \rho_j = 1. \tag{3.6}$$

The number $\rho_j \in [0, 1]$ indicates the fraction of damage residing in the damage state d_j (3.3). Initially, we have $\rho_0 = 1$ and all other ρ_j's vanish.
For any such damage-distribution state $\boldsymbol{\rho}$, the effective degradation function $\bar{f}$ computes as

$$\bar{f}(\boldsymbol{\rho}) \equiv \left(\sum_{j=0}^{N} \rho_j\, g_j\right)^{-1} \quad \text{where} \quad g_j = f(d_j)^{-1}, \tag{3.7}$$

and the associated free energy reads

$$\psi(\boldsymbol{\varepsilon}, \boldsymbol{\rho}) = \bar{f}(\boldsymbol{\rho}) \frac{1}{2}\, \boldsymbol{\varepsilon} \cdot \mathbb{C}[\boldsymbol{\varepsilon}] \tag{3.8}$$

with corresponding stress tensor

$$\boldsymbol{\sigma} \equiv \frac{\partial \psi}{\partial \boldsymbol{\varepsilon}}(\boldsymbol{\varepsilon}, \boldsymbol{\rho}), \quad \text{i.e.,} \quad \boldsymbol{\sigma} = \bar{f}(\boldsymbol{\rho})\, \mathbb{C}[\boldsymbol{\varepsilon}], \tag{3.9}$$

compare Eq. (2.9). The change from one time step to the next is governed by a suitable dissipation distance. More precisely, the transition from the internal-variable state at the previous step $\boldsymbol{\rho}^k$ to the value at the current time step $\boldsymbol{\rho}^{k+1} \equiv \boldsymbol{\rho}$ is handled via suitable mixing coefficients

$$\phi_j \in [0, 1], \quad j = 0, 1, \dots, N-1, \tag{3.10}$$

which we collect in a vector $\boldsymbol{\phi} \in [0, 1]^N$. Then, the damage fractions at the next time step are parameterized as follows

$$\rho_j(\boldsymbol{\phi}) = \begin{cases} (1-\phi_0)\rho_0^k, & j = 0, \\ (1-\phi_j)\rho_j^k + \phi_{j-1}\,\rho_{j-1}^k, & 0 < j < N, \\ \rho_N^k + \phi_{N-1}\,\rho_{N-1}^k, & j = N. \end{cases} \tag{3.11}$$

Thus, the volume fractions (3.10) determine the fraction of damage "mass" which is transferred to the next higher level, see Fig. 4 for an illustration. For a fixed level j, there is a fraction ϕ_{j-1} coming from the previous level and a fraction $1 - \phi_j$ of remaining "mass". The lowest and the highest level with indices $j = 0$ and $j = N$ deserve a special treatment. As there is no negative state, the lowest level $j = 0$ does not receive any "inflow" of damage. Thus, it can only lose damage "mass". The highest level, on the other hand, cannot lose damage "mass". Thus, there is no outflow of damage to a higher level, explaining why the index j in Eq. (3.10) runs only up to the limit $N - 1$. An example for the evolution of a discrete damage distribution with three damage values is shown in Fig. 4 for two time steps.
The dissipation distance between the damage states $\boldsymbol{\rho}^k$ and $\boldsymbol{\rho} \equiv \boldsymbol{\rho}^{k+1}$ is actually a function of the transition coefficients (3.10)

$$\mathcal{D}(\boldsymbol{\phi}) = r \sum_{j=0}^{N-1} \rho_j^k\, \phi_j\, \Delta d_j \quad \text{with} \quad \Delta d_j = d_{j+1} - d_j. \tag{3.12}$$

In view of Eq. (3.11), the dissipation (3.12) encodes the fraction of damage "mass" which dissipates to the next damage level, parameterized by the transition fractions $\boldsymbol{\phi}$.
All in all, the incremental potential P for the kth load step takes the form

$$P(\boldsymbol{\varepsilon}, \boldsymbol{\phi}) = \left(\sum_{j=0}^{N} \rho_j(\boldsymbol{\phi})\, g_j \right)^{-1} \frac{1}{2}\, \boldsymbol{\varepsilon} \cdot \mathbb{C}[\boldsymbol{\varepsilon}] + r \sum_{j=0}^{N-1} \rho_j^k\, \phi_j\, \Delta d_j, \tag{3.13}$$

where $\boldsymbol{\varepsilon} \in \mathrm{Sym}(n)$ denotes a strain tensor, the damage "masses" $\boldsymbol{\rho}$ are parameterized by Eq. (3.11) and the transition fractions $\boldsymbol{\phi}$ are elements of the unit cube (3.10). The discrete evolution of the internal variables, the damage "masses", is thus governed by the optimization problem

$$\psi_{\mathrm{cond}}(\boldsymbol{\varepsilon}) = \min_{\boldsymbol{\phi} \in [0,1]^N} P(\boldsymbol{\varepsilon}, \boldsymbol{\phi}), \tag{3.14}$$

where the minimum of the functional is the condensed incremental energy ψ_{cond}, see Eqs. (2.34) and (2.43). Notice that we drop the superscript c and the bar over the strain for notational convenience.

3.2. Computational aspects on material-point level

Algorithm 1 Evaluation of the OT damage model on material point level.

Input: current strain $\boldsymbol{\varepsilon}$, damage masses $\boldsymbol{\rho}^k$ of the previous time step
Parameters of the damage model: d, g, r ▷ Eqs. (3.2), (3.7) and (2.2)
1 Initialize the damage volume fractions $\boldsymbol{\phi} = \mathbf{0}$
2 Compute the undamaged elastic energy $\psi_0(\boldsymbol{\varepsilon})$ ▷ Eq. (2.17)
3 Compute $\boldsymbol{\xi}$ and $\boldsymbol{\eta}$ ▷ Eqs. (3.17) and (3.19)
4 **while** $\|\Delta\boldsymbol{\phi}\| > 10^{-8}$ **do**
5 Update the damage fractions $\boldsymbol{\rho}(\boldsymbol{\phi})$ ▷ Eq. (3.11)
6 Compute the effective degradation $\bar{f}(\boldsymbol{\phi})$ ▷ Eq. (3.15)
7 Update the damage volume fractions $\boldsymbol{\phi}$ ▷ Eqs. (3.29) and (3.30)
8 Compute the stress $\boldsymbol{\sigma}(\boldsymbol{\varepsilon}, \boldsymbol{\rho})$ ▷ Eq. (3.9)
Output: current stress $\boldsymbol{\sigma}$, damage masses $\boldsymbol{\rho}$ of the current time step

For a computational treatment of the model (3.14), the following remarks are helpful.

1. The effective degradation function $\bar{f}$ may be re-written in the form

$$\begin{aligned} \bar{f}(\boldsymbol{\phi}) \equiv \left(\sum_{j=0}^{N} \rho_j(\boldsymbol{\phi})\, g_j \right)^{-1} &= \left(\sum_{j=0}^{N-1} \Big((1-\phi_j)\rho_j^k\, g_j + \phi_j \rho_j^k\, g_{j+1} \Big) + \rho_N^k g_N \right)^{-1} \\ &= \left(\sum_{j=0}^{N} \rho_j^k\, g_j + \sum_{j=0}^{N-1} \phi_j \rho_j^k \big(g_{j+1} - g_j \big) \right)^{-1}, \end{aligned} \tag{3.15}$$

   which we may also express in the compressed form

$$\bar{f}(\boldsymbol{\phi}) = \big(\bar{f}(\mathbf{0})^{-1} + \boldsymbol{\phi} \cdot \boldsymbol{\xi} \big)^{-1} \tag{3.16}$$

   in terms of the vector $\boldsymbol{\xi} \in \mathbb{R}^N$ with non-negative components

$$\xi_j = \rho_j^k\, (g_{j+1} - g_j), \quad j = 0, 1, \dots, N-1. \tag{3.17}$$

2. Similarly, the dissipation distance may be expressed in the form

$$r \sum_{j=0}^{N-1} \rho_j^k\, \phi_j\, \Delta d_j = \boldsymbol{\phi} \cdot \boldsymbol{\eta} \tag{3.18}$$

   with the vector $\boldsymbol{\eta} \in \mathbb{R}^N$ whose components read

$$\eta_j = r \rho_j^k\, \Delta d_j, \quad j = 0, 1, \dots, N-1. \tag{3.19}$$

   These components are non-negative, as well.

Thus, in terms of the undamaged elastic energy ψ_0, see Eq. (2.17), the optimization problem (3.14) may be written in the compact vector form

$$P(\boldsymbol{\varepsilon}, \boldsymbol{\phi}) = \big(\bar{f}(\mathbf{0})^{-1} + \boldsymbol{\phi} \cdot \boldsymbol{\xi} \big)^{-1} \psi_0(\boldsymbol{\varepsilon}) + \boldsymbol{\phi} \cdot \boldsymbol{\eta} \to \min_{\boldsymbol{\phi} \in [0,1]^N}. \tag{3.20}$$

To derive the necessary (and sufficient) conditions for this optimization problem, we first take a look at the derivatives of the effective degradation function (3.15). This task is handled easily by re-writing Eq. (3.16) in the form

$$\frac{1}{\bar{f}(\boldsymbol{\Phi})} = \frac{1}{\bar{f}(\mathbf{0})} + \boldsymbol{\Phi} \cdot \boldsymbol{\xi}. \tag{3.21}$$

Differentiating both hands of the identity w.r.t. the variable ϕ_j, we arrive at the equation

$$-\frac{1}{\bar{f}(\boldsymbol{\Phi})^2}\frac{\partial \bar{f}(\boldsymbol{\Phi})}{\partial \phi_j} = \xi_j, \tag{3.22}$$

i.e., we are led to the expression

$$\frac{\partial \bar{f}(\boldsymbol{\Phi})}{\partial \phi_i} = -\xi_i\, \bar{f}(\boldsymbol{\Phi})^2, \quad i = 0, 1, \dots, N-1. \tag{3.23}$$

For the second derivative, we deduce

$$\frac{\partial \bar{f}(\boldsymbol{\Phi})}{\partial \phi_i\, \partial \phi_j} = -2\,\xi_i \bar{f}(\boldsymbol{\Phi})\frac{\partial \bar{f}(\boldsymbol{\Phi})}{\partial \phi_j} = 2\,\xi_i\,\xi_j\,\bar{f}(\boldsymbol{\Phi})^3, \quad i, j = 0, 1, \dots, N-1. \tag{3.24}$$

We observe that the Hessian of the objective function (3.20)

$$\frac{\partial^2 P(\boldsymbol{\varepsilon}, \boldsymbol{\Phi})}{\partial \boldsymbol{\Phi}^2} = 2\,\bar{f}(\boldsymbol{\Phi})^3 \psi_0(\boldsymbol{\varepsilon})\, \boldsymbol{\xi} \otimes \boldsymbol{\xi} \tag{3.25}$$

is a positive semi-definite matrix. Indeed, both the degradation function (3.15) and the undamaged free energy (2.17) take non-negative values, and a dyadic product of a vector leads to a positive semi-definite matrix.

The positive semidefiniteness of the Hessian (3.25) reveals that the objective function P is convex in the argument $\boldsymbol{\Phi}$. In particular, every critical point of the optimization problem (3.14) is a global minimum. We derived this fact by more general arguments in Section 2.4, but come across it at this point, as well.

To find a critical point of the problem (3.14), we first study the case of an interior critical point. Such a point satisfies the equation

$$\mathbf{0} \overset{!}{=} \frac{\partial P(\boldsymbol{\varepsilon}, \boldsymbol{\Phi})}{\partial \boldsymbol{\Phi}} = -\bar{f}(\boldsymbol{\Phi})^2 \psi_0(\boldsymbol{\varepsilon})\, \boldsymbol{\xi} + \boldsymbol{\eta}. \tag{3.26}$$

Apparently, such an interior critical point can only exist in case the vectors $\boldsymbol{\xi}$ and $\boldsymbol{\eta}$ are collinear. Still, to find a root of the vector field on the right-hand side (3.26), we take a look at a Newton-type method

$$\mathbf{0} \overset{!}{=} -\bar{f}(\boldsymbol{\Phi} + \Delta\boldsymbol{\Phi})^2 \psi_0(\boldsymbol{\varepsilon})\, \boldsymbol{\xi} + \boldsymbol{\eta} \approx -\bar{f}(\boldsymbol{\Phi})^2 \psi_0(\boldsymbol{\varepsilon})\, \boldsymbol{\xi} + \eta + 2\,\bar{f}(\boldsymbol{\Phi})^3\, \psi_0(\boldsymbol{\varepsilon})(\boldsymbol{\xi} \otimes \boldsymbol{\xi})\Delta\boldsymbol{\Phi}, \tag{3.27}$$

i.e.,

$$(\boldsymbol{\xi} \otimes \boldsymbol{\xi})\Delta\boldsymbol{\Phi} = \frac{\bar{f}(\boldsymbol{\Phi})^2 \psi_0(\boldsymbol{\varepsilon})\, \boldsymbol{\xi} - \boldsymbol{\eta}}{2\,\bar{f}(\boldsymbol{\Phi})^3\, \psi_0(\boldsymbol{\varepsilon})}. \tag{3.28}$$

Due to the degeneracy of the left-hand side, we consider the diagonal components of the matrix $\boldsymbol{\xi} \otimes \boldsymbol{\xi}$ only. To account for the box constraints $0 \le \phi_j \le 1$, we use a projection onto the interval $[0, 1]$. We are thus led to the update scheme

$$\phi_j \leftarrow \max\Big(0, \min\Big(\phi_j + s_j\Big(\bar{f}(\boldsymbol{\Phi})^2 \psi_0(\boldsymbol{\varepsilon})\, \xi_j - \eta_j\Big), 1\Big)\Big), \quad j = 0, 1, \dots, N-1, \tag{3.29}$$

with the step size

$$s_j = \begin{cases} \left(2\,\bar{f}(\boldsymbol{\Phi})^3\, \psi_0(\boldsymbol{\varepsilon})\, \xi_j^2\right)^{-1}, & \rho_j^k > 0, \\ 0, & \text{otherwise.} \end{cases} \tag{3.30}$$

Put differently, we consider a projected gradient method [95, 16.6] with an adaptive step size which recovers Newton's method in 1D. The algorithmic approach is summarized in Algorithm 1. The designed computational treatment is simple, yet resolves the incremental problem (3.14) quickly. In the computational practice, we observe convergence of the numerical scheme to a unique fixed point. We do not, however, have a mathematical argument for uniqueness at our disposal.

3.3. Convexity properties of the condensed incremental energy

In this section, we take a look at the mathematical properties of the condensed incremental energy (3.14)

$$\psi_{\text{cond}}(\boldsymbol{\varepsilon}) = \min_{\boldsymbol{\Phi} \in [0,1]^N} P(\boldsymbol{\varepsilon}, \boldsymbol{\Phi}), \quad \boldsymbol{\varepsilon} \in \text{Sym}(n), \tag{3.31}$$

with the incremental potential (3.13)

$$P(\boldsymbol{\varepsilon}, \boldsymbol{\Phi}) = \left(\sum_{j=0}^{N} \rho_j(\boldsymbol{\Phi})\, g_j\right)^{-1} \frac{1}{2}\, \boldsymbol{\varepsilon} \cdot \mathbb{C}[\boldsymbol{\varepsilon}] + r \sum_{j=0}^{N-1} \rho_j^k\, \phi_j\, \Delta d_j, \tag{3.32}$$

which governs the mechanical subproblem associated to each discrete time step with the parametrization (3.11). The condensed incremental energy has the following properties:

(i) There are positive constants α_-, α_+ and C_+, s.t. the two-sided estimate

$$\frac{\alpha_-}{2}\,\boldsymbol{\varepsilon}\cdot\mathbb{C}[\boldsymbol{\varepsilon}] \le \psi_{\mathrm{cond}}(\boldsymbol{\varepsilon}) \le C_+ + \frac{\alpha_+}{2}\,\boldsymbol{\varepsilon}\cdot\mathbb{C}[\boldsymbol{\varepsilon}] \tag{3.33}$$

is valid for all strains $\boldsymbol{\varepsilon} \in \mathrm{Sym}(n)$.

(ii) The condensed incremental energy (3.31) is convex, but not strictly convex.

(iii) The naturally associated mechanical boundary-value problem admits minimizers. More precisely, suppose a domain $\Omega \subseteq \mathbb{R}^n$ is given, whose sufficiently smooth boundary

$$\partial\Omega = \Gamma_D \cup \Gamma_N \tag{3.34}$$

decomposes into non-overlapping subsets Γ_D and Γ_N which serve as the locations where Dirichlet and Neumann boundary conditions are imposed. In case the function

$$H^1_D(\Omega)^n \to \mathbb{R}, \quad \boldsymbol{u} \mapsto \|\boldsymbol{u}\|_{H^1_D} := \|\nabla^s \boldsymbol{u}\|_{L^2}, \tag{3.35}$$

defines a norm on the Sobolev space

$$H^1_D(\Omega)^n = \left\{ \boldsymbol{u} \in H^1(\Omega) \,\middle|\, \boldsymbol{u}\big|_{\Gamma_D} \equiv \boldsymbol{0} \right\} \tag{3.36}$$

with vanishing trace on the Dirichlet boundary, for any boundary-condition enforcing displacement field $\boldsymbol{u}_0 \in H^1(\Omega)^n$, body-force field $\boldsymbol{f} \in H^{-1}_D(\Omega)^n \equiv \left(H^1_D(\Omega)^n\right)'$ and traction field $\boldsymbol{t} \in H^{-\frac{1}{2}}(\Gamma_N)^n$, there is a minimizer to the variational problem

$$\int_\Omega \psi_{\mathrm{cond}}(\nabla^s(\boldsymbol{u}_0 + \boldsymbol{u})) + \boldsymbol{f}\cdot\boldsymbol{u}\,\mathrm{d}V + \int_{\Gamma_N} \boldsymbol{t}\cdot\boldsymbol{u}\,\mathrm{d}A \longrightarrow \min_{\boldsymbol{u}\in H^1_D(\Omega)^n}. \tag{3.37}$$

The first property (3.33) ensures that the incremental energy is sandwiched between two quadratic functions, ensuring both a coercivity condition and a growth estimate. Together with the second property, the weak lower semicontinuity of the functional (3.37) is ensured, see standard textbooks on the calculus of variations like Dacorogna [62]. In particular, these two properties are responsible for the validity of the third statement, i.e., the existence of minimizers to the mechanical boundary problem (3.37), associated to each time step of a component made of a homogeneous OT damage material. A simple sufficient condition for the uniqueness of solutions to the problem (3.37) is strict convexity. Such a condition is not satisfied by the incremental energy (3.31), as stated in condition (ii) and demonstrated explicitly for the first time step in Appendix C.3.

For the sake of readability, the arguments supporting the claimed properties (i)–(iii) were out-sourced to Appendix C.

4. Computational investigations

4.1. Setup

We consider matrix-inclusion materials within a fixed unit cell

$$Q = [0, Q_1] \times [0, Q_2] \times [0, Q_3], \tag{4.1}$$

i.e., we suppose that two open subsets – corresponding to the matrix and the inclusion – are given, which are disjoint and whose closure covers the entire cell. Then, we consider heterogeneous generalized standard materials, s.t. the fibers are purely elastic and the matrix is governed by a damageable material. More precisely, we consider different material models, encompassing the original damage model (2.1)-(2.2) (with $\dot{d}_{\max} = +\infty$), the rate-limitation approach (2.1)-(2.2) (with $\dot{d}_{\max} < +\infty$) proposed by Allix [63], the relaxation-type model by Schwarz et al. [59] and the novel optimal transport (OT) model introduced in the manuscript at hand, and discussed in Section 3.

Within every time step, kinematic compatibility enforces the local strain field within the unit cell to possess the form

$$\boldsymbol{\varepsilon}(\boldsymbol{x}) = \bar{\boldsymbol{\varepsilon}} + \nabla^s \boldsymbol{u}(\boldsymbol{x}), \quad \boldsymbol{x} \in Q, \tag{4.2}$$

involving the symmetrized gradient of a periodic displacement-fluctuation field $\boldsymbol{u}$. In particular, the macroscopic strain $\bar{\boldsymbol{\varepsilon}}$ computes as the volume average of the microscopic strain field $\boldsymbol{\varepsilon}$

$$\bar{\boldsymbol{\varepsilon}} = \frac{1}{Q_1 Q_2 Q_3} \int_Q \boldsymbol{\varepsilon}(\boldsymbol{x})\,\mathrm{d}V. \tag{4.3}$$

We assume the material to be undamaged in the initial state. For a prescribed loading path of macroscopic strains $\bar{\boldsymbol{\varepsilon}}$, we seek, for each time step, the associated strain field (4.2) and field of damage variables, s.t. the static balance of linear momentum without volume forces

$$\mathrm{div}\,\boldsymbol{\sigma}(\boldsymbol{x}) = \boldsymbol{0} \tag{4.4}$$

is satisfied, where the stress tensor is related to the strain tensor and the internal variables through the governing constitutive law. Subsequently, the macroscopic stress tensor $\bar{\boldsymbol{\sigma}}$ arises via volume averaging [96]

$$\bar{\boldsymbol{\sigma}} = \frac{1}{Q_1 Q_2 Q_3} \int_Q \boldsymbol{\sigma}(\boldsymbol{x})\,\mathrm{d}V. \tag{4.5}$$

Table 1
Isotropic material properties for the PA matrix and the E-glass fibers, both taken from Doghri et al. [104].

E-glass fibers	PA matrix
$E = 72.0$ GPa	$E = 2.1$ GPa
$\nu = 0.22$	$\nu = 0.3$

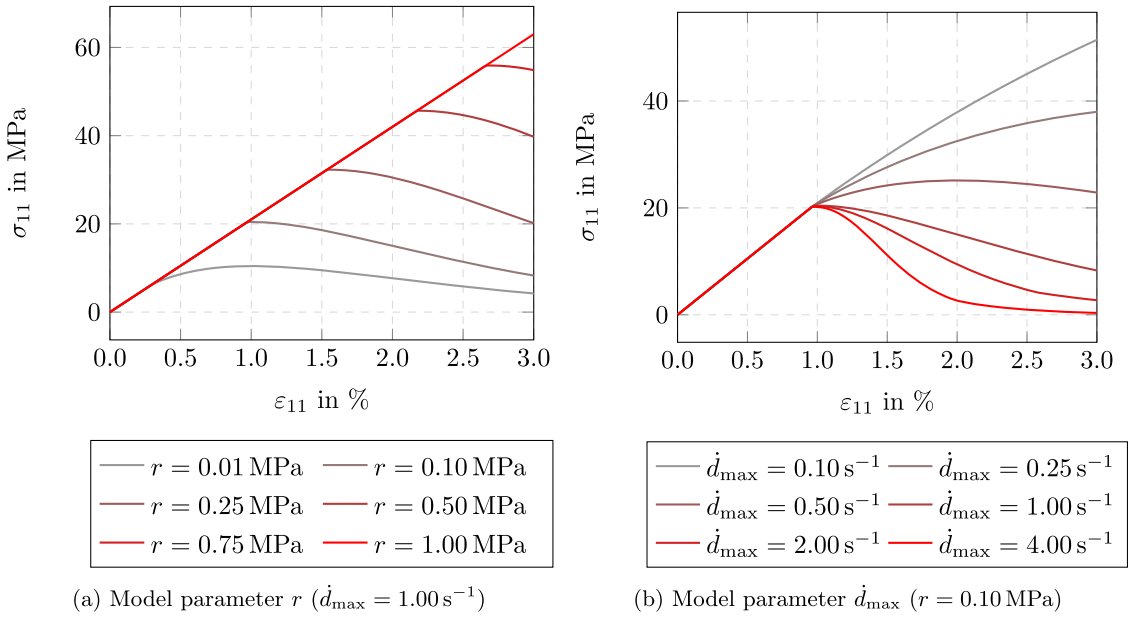

(a) Model parameter r ($\dot{d}_{\max} = 1.00\,\mathrm{s}^{-1}$) (b) Model parameter $\dot{d}_{\max}$ ($r = 0.10\,\mathrm{MPa}$)

Fig. 5. Stress-strain curve for varying model parameters on material point level.

To solve the static balance of linear momentum (4.4), we use an implementation of the proposed damage model as a user-defined subroutine within an FFT-based computational homogenization code. The code [97,98] is written in Python with Cython extensions and parallelized with OpenMP. For the numerical homogenization within the FFT-based computational homogenization framework [75,76], we discretize the problem by finite differences on a staggered grid [99]. The resulting nonlinear equations are solved with a conjugate gradient scheme [100–103] with a relative tolerance of 10^{-5} as termination criterion. The investigations were conducted on a desktop computer equipped with an 8-core Intel i7 CPU, 64 GB RAM, and enabled Hyper-Threading with a total number of 16 threads. For the computations related to the long fiber reinforced composite material at the end of the computational investigations, we used a workstation with two AMD EPYC 9534 CPUs, each with 64 physical cores, enabled SMT, 256 threads total, and 1024 GB of DRAM.

As the standard material, we consider a polyamide (PA) matrix reinforced with E-glass fibers. For the matrix material and the fibers, we use isotropic elastic parameters [104], see Table 1. Whereas the fibers are modeled in a purely linear elastic way, we apply the introduced damage model to the matrix material and define the damage parameters r and $\dot{d}_{\max}$ as part of the considered studies.

We limit the minimum of the effective degradation function $\bar{f}$ to be greater or equal than the threshold 10^{-10}, which leads to a maximum damage $d_{\max} \approx 23.03$ for the exponential degradation function, $d_{\max} = 1 - 10^{-10}$ for the linear degradation function and $d_{\max} \approx 0.99999$ for the quadratic degradation function. If not specified otherwise, the exponential degradation function is used for the damage model at hand.

4.2. Studies on material point level

In this section, we investigate the influence of the damage parameters r and $\dot{d}_{\max}$ as well as the degradation-function type on the damage model. Therefore, we investigate the stress-strain behavior of the matrix material at material point level. As the loading condition, we select an uniaxial extension in $\boldsymbol{e}_1$-direction with maximum strain of $\varepsilon_{11} = 3\,\%$. The loading is applied in 200 linear loading steps with a time increment of $\Delta t = 0.015\,\mathrm{s}$. As the standard setup, we select the damage parameters $r = 0.10\,\mathrm{MPa}$ and $\dot{d}_{\max} = 1.00\,\mathrm{s}^{-1}$.

Influence of the damage parameters

Let us start with the investigation of the model parameter r. According to Eq. (2.16), the undamaged energy ψ_0 needs to be greater or equal to the value r for damage to initiate in case of an exponential degradation function. As the undamaged energy computes as

$$\psi_0(\boldsymbol{\varepsilon}) = \frac{1}{2} E \varepsilon_{11}^2 \tag{4.6}$$

for the considered unidirectional tensile test, damage starts at the applied strain level

$$\varepsilon_{11} = \sqrt{\frac{2r}{E}}. \tag{4.7}$$

Thus, the model parameter r may be interpreted as a limit for damage initiation. The obtained stress-strain curves for varying model parameters r are given in Fig. 5(a). In accordance with Eq. (4.7), we observe that with increasing parameter r, the damage initiation is activated at a higher strain level ε_{11}. For instance, the required strain with respect to damage initiation is $\varepsilon_{11} \approx 0.31\,\%$ for the parameter $r = 0.01$ MPa and $\varepsilon_{11} \approx 2.67\,\%$ for the parameter $r = 0.75$ MPa. In fact, for the highest parameter value $r = 1.00$ MPa investigated, the required strain is above the maximum strain of $\varepsilon_{11} = 3\,\%$, i.e., the material shows a completely linear elastic behavior within the considered range.

For the smallest considered parameter value $r = 0.01$ MPa, taking a look beyond the elastic region, we observe first a positive slope, i.e., a region of hardening, and then a negative slope, i.e., softening. In all other cases, no significant initial hardening is observable. Let us compute the critical value for r which marks the transition from hardening to softening at the damage initiation. To simplify the discussion, we investigate the non-convex damage model instead of the OT damage model. At the start of the damage initiation (4.7), the corresponding stress level reads

$$\sigma_{11}^k(\varepsilon_{11}^k) = \sqrt{2\,r\,E}, \tag{4.8}$$

where k denotes the time step of the damage initiation. For the strain increment $\Delta\varepsilon_{11}$, the strain level of the subsequent time step becomes

$$\varepsilon_{11}^{k+1} = \varepsilon_{11}^k + \Delta\varepsilon_{11}, \tag{4.9}$$

and the damage variable increases from zero to the value $d^{k+1}(\varepsilon_{11}^{k+1})$. Using the formula for the damage evolution (2.16) and the positivity of the increment $\Delta\varepsilon_{11}$, the stress at the subsequent time step follows:

$$\sigma_{11}^k(\varepsilon_{11}^k) \equiv f(d^{k+1})\,E\,\varepsilon_{11}^{k+1} = f(d^{k+1})\,E(\varepsilon_{11}^k + \Delta\varepsilon_{11}). \tag{4.10}$$

The stress-strain curve shows hardening if and only if σ_{11}^k is smaller than σ_{11}^{k+1} and softening otherwise. Thus, the condition

$$f(d^{k+1})\,E\,\Delta\varepsilon_{11} - \sqrt{2\,r\,E}\,(1 - f(d^{k+1})) = 0 \tag{4.11}$$

characterizes the transition between hardening and softening behavior. For the considered study setup, the nonlinear Eq. (4.11) is satisfied for the model parameter $r \approx 0.103$, i.e., only the two smallest parameter selections start with hardening, confirming our computational observations.

The influence of the model parameter $\dot{d}_{\max}$ on the stress-strain behavior of the damage model is shown in Fig. 5(b). As we fix the model parameter r, all models leave the linear elastic regime at the same level. After the damage onset, the model parameter $\dot{d}_{\max}$ affects the shape of the curve. For small parameters $\dot{d}_{\max}$, the damage progression is limited in a stronger way, and thus the stiffness degradation is less pronounced. For the models with the parameter values $\dot{d}_{\max} = 0.10\,\mathrm{s}^{-1}$ and $\dot{d}_{\max} = 0.25\,\mathrm{s}^{-1}$, we observe a large region of hardening, but no softening. However, these models would also include a softening behavior in case of higher applied strains. With increasing rate limit $\dot{d}_{\max}$, the stiffness reduction gets more apparent, the region of hardening decreases and a pronounced softening behavior is observed.

In addition, we study the influence of the model parameter $\dot{d}_{\max}$ on the realized damage distribution, see Fig. 6. For the three considered maximum damage rates, the unloaded material is completely undamaged, i.e., the damage distribution takes the form $\mu = \delta_0$. For increasing applied strain, we observe that the entire damage mass propagates to the maximum damage level for each time step in Fig. 6(a), when limiting the damage rate to $\dot{d}_{\max} = 1.0\,\mathrm{s}^{-1}$. In contrast, for the two higher maximum damage rates $\dot{d}_{\max} = 2.0\,\mathrm{s}^{-1}$ and $\dot{d}_{\max} = 4.0\,\mathrm{s}^{-1}$, it turns out that the damage distributions are characterized by higher variances and that a significant fraction of the damage mass always remains undamaged, while only smaller fractions propagate to complete failure, see Fig. 6(b) and (c). These observations are caused by the definition of the effective degradation as the harmonic mean of the damage distribution. In fact, the effective degradation tends to zero in case any subset - independent of its damage fraction - tends to the maximum damage value. Transferring these insights about the harmonic mean to the minimization problem to be solved (3.14), for a fixed dissipation distance the incremental potential gets smaller in case larger damage increments are permitted (but for smaller damage fractions), compared to a scenario where the total damage is distributed over many smaller steps. As a result, transporting smaller damage fractions over larger damage increments is energetically more favorable than transporting larger fractions over smaller damage increments. As increasing the maximum damage rate $\dot{d}$ permits higher damage increments, the evolution of the damage distribution changes from transporting the total damage over many smaller steps, see Fig. 6, towards transporting decreasing damage fractions over increasing damage steps, see Fig. 6(b) and (c). Consequently, an increasing damage mass remains at low damage states. For the extreme case with unlimited damage rate $\dot{d}_{\max} \to \infty$, almost the entire damage mass is concentrated at low damage states, whereas only an infinitesimal fraction propagates to the maximum damage state, which may be interpreted as damage localization.

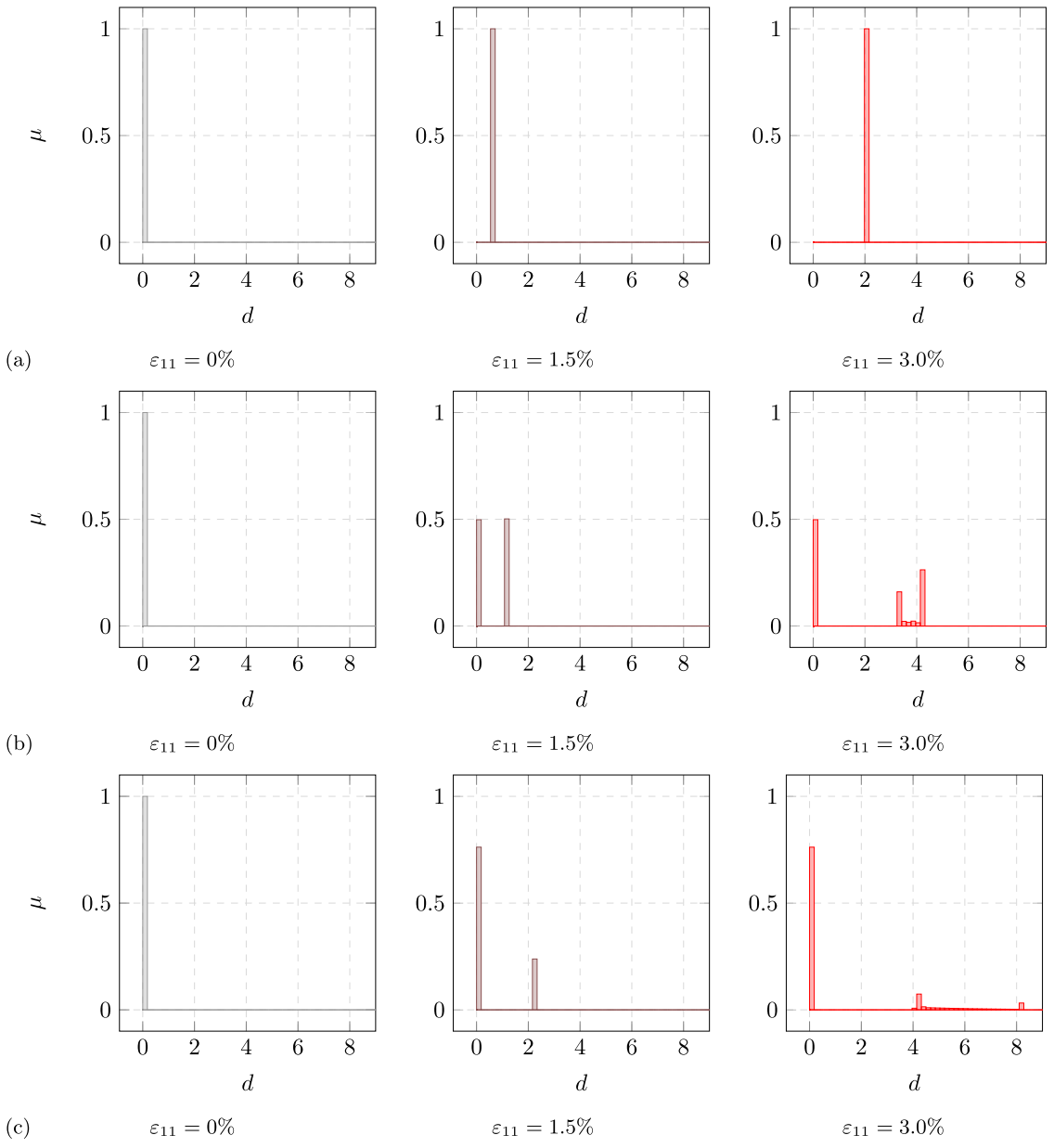

Fig. 6. Damage distribution for increasing strain levels with different enforced damage-rate limitations $\dot{d}_{\max} = 1.0\,\mathrm{s}^{-1}$ (a), $\dot{d}_{\max} = 2.0\,\mathrm{s}^{-1}$ (b) and $\dot{d}_{\max} = 4.0\,\mathrm{s}^{-1}$ (c).

Influence of the selected degradation function

Besides the model parameters, we also study the differences when using different types of degradation functions. To do so, we fix the model parameters $r = 0.1\,\mathrm{MPa}$ and $\dot{d}_{\max} = 1.0\,\mathrm{s}^{-1}$, but consider all three types of degradation functions.

In Fig. 7(a), the stress-strain curves are shown. For the linear and the exponential function, damage initiates at the energy level $\psi_0(\boldsymbol{\varepsilon}) = r$, see Eqs. (2.16) and (2.19). Thus, both curves share the linear elastic regime. In contrast, the quadratic damage function features a damage onset at the level $\psi_0(\boldsymbol{\varepsilon}) = r/2$, see Eq. (2.18), which manifests in a smaller linear elastic regime. To compare the three degradation functions with equal damage onset, we also plot the stress-strain curve for the quadratic damage function with $r = 0.2\,\mathrm{MPa}$. We observe that the damage model strongly depends on the selected damage degradation function. Whereas similar stress-strain curves with complete damage at $\varepsilon_{11} \approx 1.97\,\%$ emerge for the linear and the quadratic damage function, the exponential degradation function leads to a significantly slower stiffness degradation, and thus to higher remaining stresses.

Let us have a look at the effective degradation $\bar{f}$, see Fig. 7(b), to study the differences with respect to the remaining stiffness more thoroughly. It turns out that the exponential degradation function still leads to an effective degradation of $\bar{f} \approx 0.37$ when the material

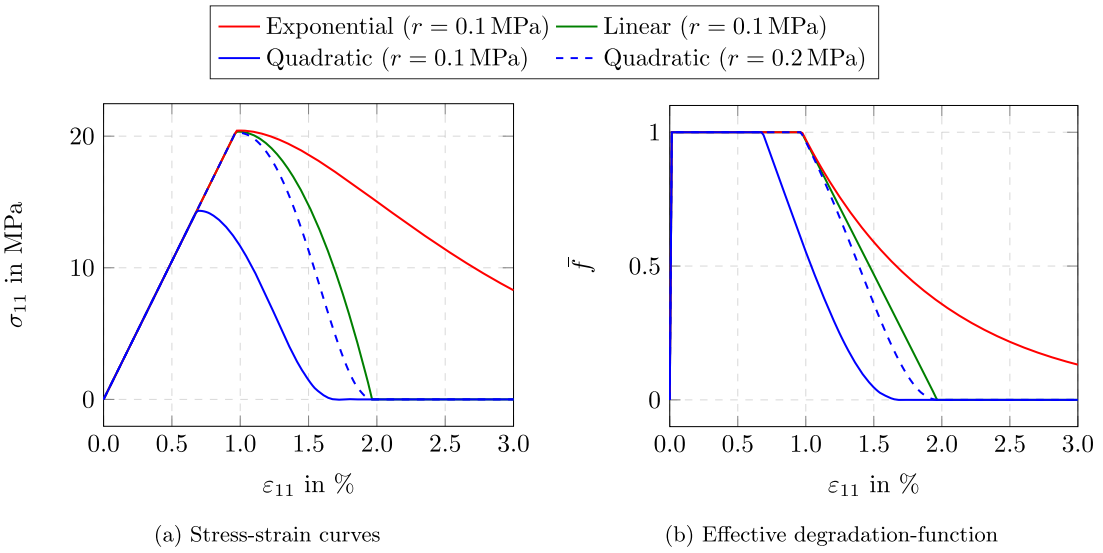

(a) Stress-strain curves (b) Effective degradation-function

Fig. 7. Comparison of three degradation functions on material point level.

already fails for the other two degradation functions. Even at the highest applied strain of $\varepsilon_{11} = 3\,\%$, about 13 % of the undamaged stiffness remains for the exponential degradation function.

The derivatives of the quadratic degradation function

$$f'(d) = -2(1-d), \quad 0 \le d \le 1, \tag{4.12}$$

and the exponential degradation function

$$f'(d) = -\exp(-d), \quad d \ge 0, \tag{4.13}$$

converge to zero for $d \to d_{\max}$. As a result, the effective degradation curves reveal an asymptotic behavior for $\varepsilon_{11} \to \varepsilon_{11}^{\text{fail}}$, where $\varepsilon_{11}^{\text{fail}}$ denotes the strain at material failure. In contrast, the derivative of the linear degradation function

$$f'(d) = \begin{cases} -1, & 0 \le d < 1, \\ 0, & d = 1, \end{cases} \tag{4.14}$$

has no convergence behavior, but is discontinuous at $d_{\max} = 1$, which transfers to the slope of the effective degradation curve.

4.3. Implications of the OT damage model for boundary value problems

To discuss the OT damage model as a constitutive model for components with heterogeneous stress states, we consider a matrix material with a single circular inclusion, which is furnished with the material parameters of E-glass, see Table 1. The diameter of the circle is assumed to be $d = 10\,\mu\text{m}$ and the quadratic unit cell has an edge length of $Q_i = 20\,\mu\text{m}$ $(i = 1, 2)$. We apply the macroscopic normal strain $\bar{\varepsilon}_{11} = 3\,\%$ via periodic boundary conditions in 100 loading steps with the time increment $\Delta t = 0.03\,\text{s}$. For the damage parameters, we use $r = 1.00\,\text{MPa}$ and $\dot{d}_{\max} = 4.00\,\text{s}^{-1}$.

On the mesh-independence of the non-convex and the OT damage model

Let us start the investigations with a study on the mesh-size effect by varying the pixel count per direction of the rectangular grid

$$N \in \{20, 40, 80, 160, 320\}. \tag{4.15}$$

We consider the non-convex damage model (2.1)-(2.2) either without or with damage rate limitation as well as the OT damage model. To obtain the results for the non-convex damage model, we used the FFT-based homogenization technique with the basic scheme [75] as the conjugate gradient solver did not converge for those material models. The mean and the standard deviation of the solver's iteration count for a single time step are shown in Table 2. We observe that the iteration count increases for refined resolutions. Due to the numerical stability of the FFT-based computational micromechanics with the OT damage model and the applicability of the superior (non-linear) conjugate gradient solver, the iteration count is significantly decreased compared to the other two damage models. The small iteration count below 240 on average highlights the improved convergence behavior of the algorithm with the OT damage model. Comparing the mean iteration number for 320^2 pixels, the non-convex damage model without damage rate limitation leads to 14 160 iterations and the non-convex damage model with damage rate limitation results in 6 876 iterations, whereas for the OT damage model 239 iterations are required, i.e., only 1.7% and 3.5% of the other two damage models, respectively.

In addition to the iteration numbers, we assess the total runtime to discuss whether the lower iteration count of the OT damage compensates for the increase in runtime due to the convexification process. The computations were conducted on a desktop computer,

Table 2
Per time-step mean and standard deviation of the solver iteration-count for a matrix material with a single circular inclusion. We compare different damage models for the matrix materials and resolutions of the composite.

Resolution	20^2	40^2	80^2	160^2	320^2
Non-convex damage ($\dot{d}_{\max} = \infty$)	1595 ± 2882	1205 ± 3935	3096 ± 9317	7567 ± 30637	14160 ± 92676
Non-convex damage ($\dot{d}_{\max} = 4.00\,\mathrm{s}^{-1}$)	696 ± 1048	2440 ± 5271	4963 ± 10521	6481 ± 16890	6876 ± 17656
ERVE damage model	401 ± 589	1415 ± 3309	2219 ± 5665	2465 ± 6727	2528 ± 6714
OT damage model	50 ± 54	89 ± 120	128 ± 195	163 ± 270	239 ± 435

see Section 4.1 for more details on the hardware configuration, using four threads. For a pixel count of 320^2, the runtime with the non-convex damage model without damage-rate limitation was about 864 min, decreasing to 483 min for the non-convex damage model with damage-rate limitation. In contrast, the OT damage model required 74 min, i.e., only 15% of the runtime of the non-convex damage model with damage-rate limitation. Thus, the study demonstrates that the reduction in the iteration number significantly outweighs the cost of the convexification process.

Besides the algorithmic convergence behavior, we also study the effect of the mesh-size on the mechanical response for the different resolutions in Fig. 8. For all damages models, we observe that the stress-strain curves of all four mesh-sizes almost coincide in the elastic regime, i.e., the results are mesh-independent.

When softening effects start, the results for the non-convex model without damage rate limitation no longer converges due to the onset of localization, which leads to mesh dependency [56], see Fig. 8(a). For the non-convex model with damage rate limitation in Fig. 8(b), we observe a converging trend, however the differences between the resolutions are still quite high. In contrast, the results for the OT damage model in Fig. 8(c) reveal a significantly improved convergence behavior. To examine the convergence behavior of the non-convex damage model with damage rate limitation and the OT damage model more closely, we analyze the absolute relative mesh-size error of the stress-strain curves compared to the finest resolution

$$\delta\bar{\sigma}_{11} = \left| \frac{\bar{\sigma}_{11,N_i} - \bar{\sigma}_{11,320}}{\bar{\sigma}_{11,320}} \right| \cdot 100\% \tag{4.16}$$

and report on the maximum of the error $\delta\bar{\sigma}_{11}$ for each pixel count in Fig. 9(a). It turns out that the error is always lower for the OT damage model compared to the non-convex damage model, which is a result of the convexification procedure. Targeting an error below 3%, we may use the resolution $N_i = 80$ for the OT damage model with a relative error of 1.22%. However, for the non-convex damage model the relative error is still 7.18% for the resolution $N_i = 80$ and 2.58% for the resolution $N_i = 160$. Thus, we need to resolve the structure with at least $N_i = 160$ pixels per axis for the non-convex damage model to ensure the convergence criterion of 3%. Due to the higher voxel count, the less stable convergence behavior and the inability to use the efficient conjugate gradient solver, the computational effort is tremendously higher for the non-convex damage model compared to the OT damage model.

To study the localization as well as the differences in the convergence behavior with respect to the damage degradation, we plot the effective degradation field $\bar{f}$ at the strain level $\bar{\varepsilon}_{11} = 3.0\,\%$ for the three damage models and varying pixel counts in Fig. 10. For the non-convex damage model without damage rate limitation, the progressive localization with decreasing voxel edge-length is clearly visible in Fig. 10(a). Due to damage rate limitation, localization is prevented in Fig. 10(b). However, in contrast to the effective degradation field of the convexified OT damage model, see Fig. 10(c), finer resolutions are necessary for an adequate approximation of the quantity, which leads to the higher error in Fig. 9(a).

The considered study may lead to the impression that the non-convex damage model with damage-rate limitation does not suffer from convergence problem under grid refinements for regular meshes. This observation may, however, be very specific to the problem at hand. There is no guarantee that this positive behavior transfers to other cases. In contrast, the convexification process of the OT damage model ensures salient mathematical properties - coercivity and (quasi-)convexity - to hold, in general.

Comparison to the damage model introduced by Schwarz et al. *[59]*

In this section, we compare the OT damage model with a damage model introduced by Schwarz et al. [59], which is also derived by applying a convexification scheme to the non-convex damage model in Eqs. (2.1)–(2.2). To approximate the convex hull, Schwarz et al. [59] model the damage variable at each material point in a microstructured fashion with n_{ERVE} discrete damage states defined on an *emulated representative volume element* (ERVE). The attained condensed incremental energy is equivalent to Eq. (2.27) with constant weighting coefficients $c_i = 1/n_{\mathrm{ERVE}}$ $(i = 1, \dots, n_{\mathrm{ERVE}})$. In addition to the parameters r and $\dot{d}_{\max}$, the number of discrete damage states n_{ERVE} needs to be selected. In this work we use $n_{\mathrm{ERVE}} = 20$, consistent with the computational investigation conducted by Schwarz et al. [59]. To solve the static balance of linear momentum (4.4), we use the FFT-based homogenization framework with the basic scheme [75] as the conjugate gradient solver failed to converge for the ERVE damage model. Due to the convexification scheme, also the ERVE damage model shows a favorable convergence behavior with respect to mesh refinement, see Figs. 8(d) and 9(a). In addition, the iteration count is decreased compared due to the non-convex damage models, see Table 2, but increased compared to the OT damage model. Having a look at the runtime of 466 min for the pixel count of 320^2, we observe that the computational cost of the ERVE damage model is between the costs of the non-convex damage models and of the OT damage model.

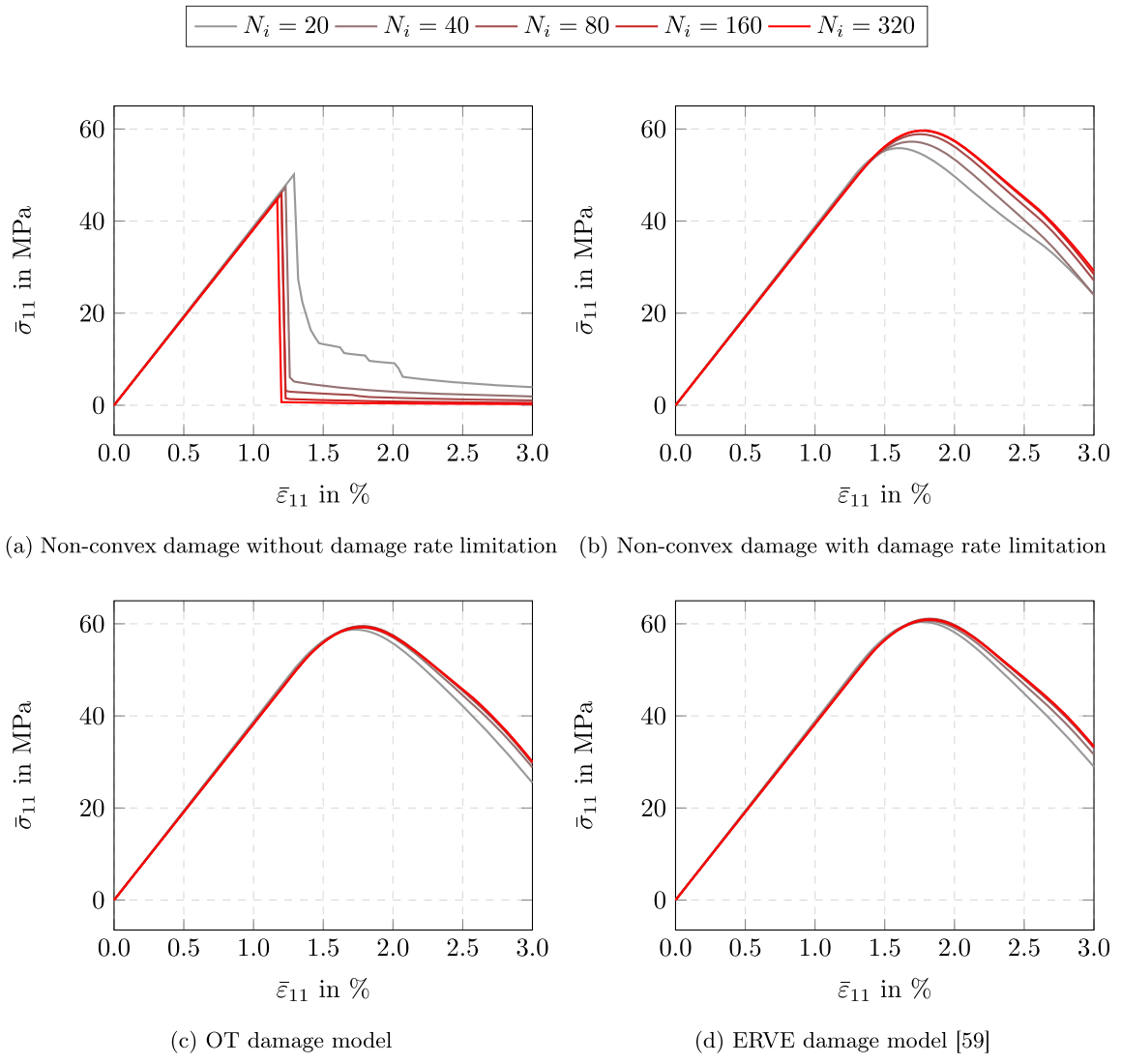

(a) Non-convex damage without damage rate limitation (b) Non-convex damage with damage rate limitation

(c) OT damage model (d) ERVE damage model [59]

Fig. 8. Mesh size study for different models and pixel counts for the circular inclusion.

In Fig. 9(b), we plot the stress-strain curves for both convexified damage models as well as for the non-convex damage model with damage rate limitation, using a pixel count of $N_i = 320$ per axis. We observe that the non-convex damage model and the OT damage model lead to almost coinciding curves, i.e., the convexification process does not alter the stress-strain behavior significantly. For the ERVE damage model, the convexification process has a greater influence on the results, leading to a slightly higher predicted stress-strain response compared to the other two damage models.

4.4. Validation of the representativity for stochastic homogenization

In this section, we apply the OT damage model to discontinuously fiber-reinforced composites, which exhibit a heterogeneous and random microstructure, to investigate the representativity of the predicted material behavior within the framework of stochastic homogenization. We use the material data summarized in Table 1 for the matrix material and the fibers, and select the damage parameters $r = 1.00\,\text{MPa}$ and $\dot{d}_{\max} = 4.00\,\text{s}^{-1}$.

For the periodic microstructure generation, we use the fused sequential addition and migration (fSAM) algorithm [105,106]. The synthetic packings are filled with a fiber volume fraction of $\phi = 20\,\%$. We model the fibers as polygonal chains with the fiber length $L = 1000\,\mu\text{m}$, the constant fiber diameter $D = 10\,\mu\text{m}$ and a maximum segment length $\bar{\ell} = 25\,\mu\text{m}$. To avoid extremely high angles between adjacent segments, we prescribe the maximum curvature $\bar{\kappa} = 0.02\,\mu\text{m}^{-1}$. Additionally, we choose a minimum distance between the fibers of 20 % of the fiber diameter, i.e., $2.0\,\mu\text{m}$. For the fiber orientation tensor [107] of second order, we target the tensor $\boldsymbol{A} \mathrel{\hat{=}} \texttt{diag}(0.75, 0.15, 0.1)$, and use the exact closure to approximate the fiber orientation tensor of fourth order [108,109]. The

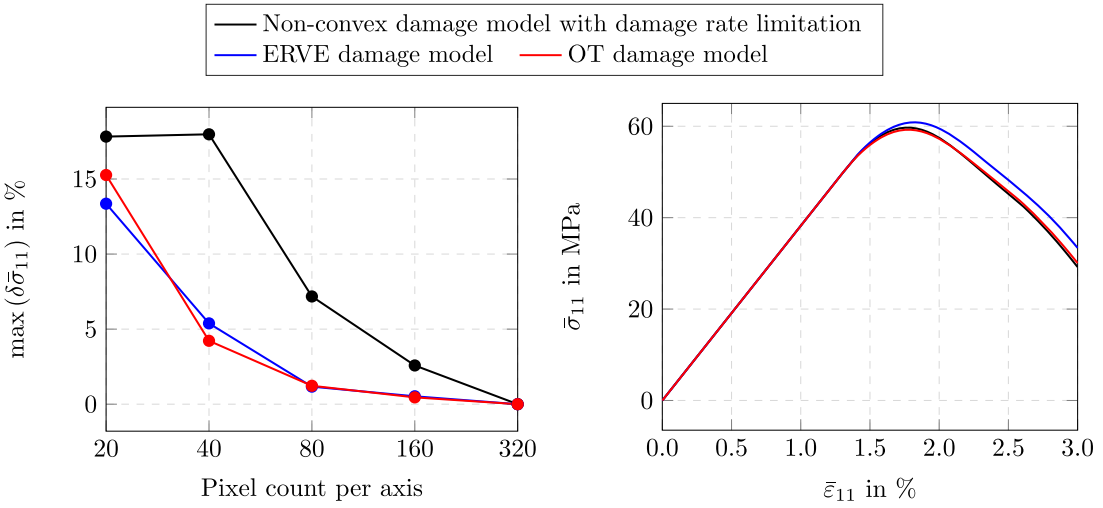

(a) Maximum relative mesh-size error (b) Stress-strain curve ($N_i = 320$)

Fig. 9. Comparing stress-strain curves and errors for the non-convex damage model with damage rate limitation, the OT damage model and the ERVE damage model [59] for the circular inclusion.

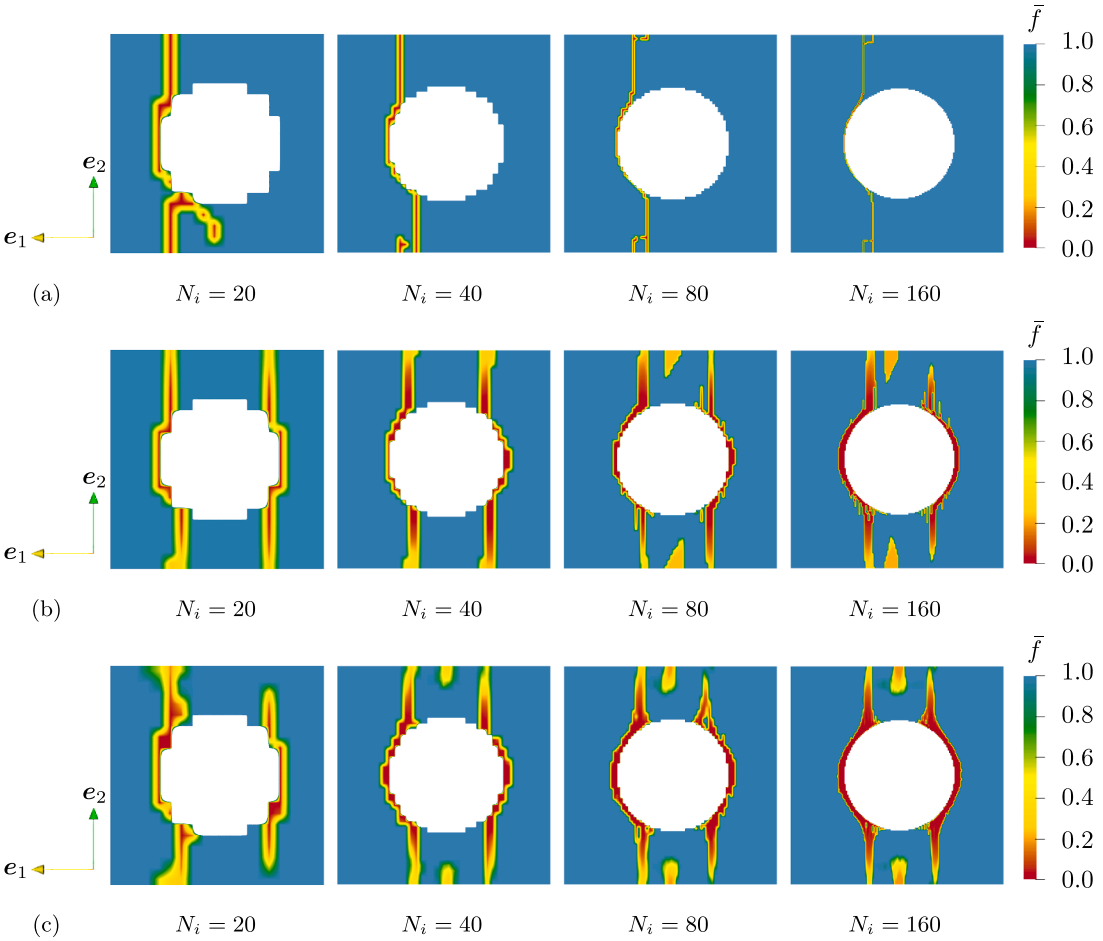

Fig. 10. Distribution of the effective degradation for varying resolutions, using the non-convex damage model without damage rate limitation (a), the non-convex damage model with damage rate limitation (b) and the OT damage model (c) for the circular inclusion.

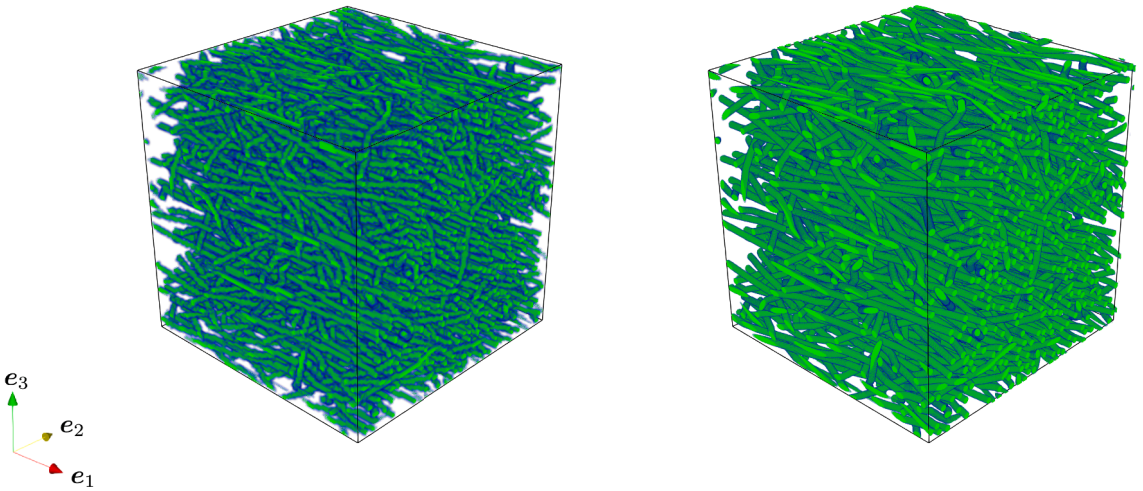

(a) $h = 4.00\,\mu\text{m}$ (b) $h = 1.00\,\mu\text{m}$

Fig. 11. Fiber microstructure resolved with two different voxel-edge lengths h.

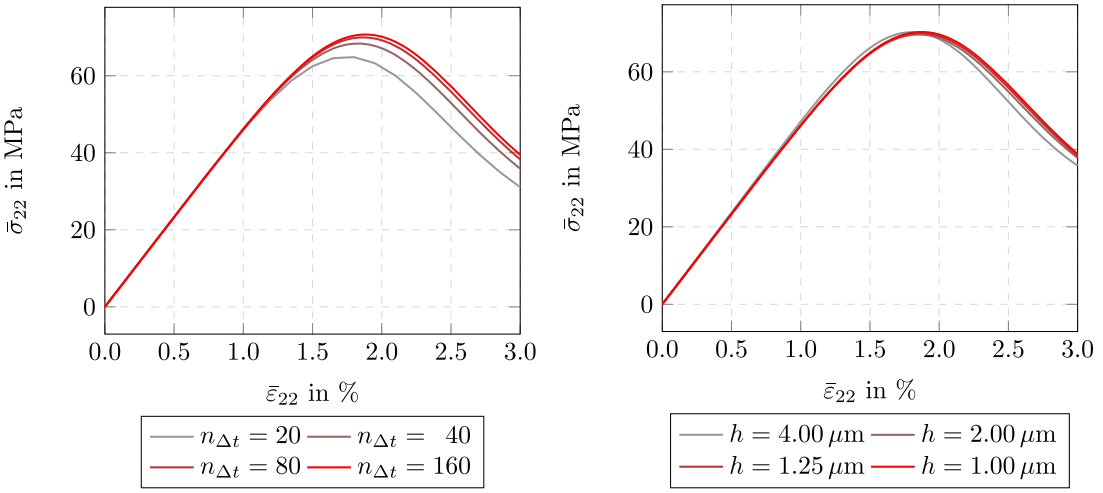

(a) With respect to the time-step size (b) With respect to the spatial resolution

Fig. 12. Sensitivity studies of the stress-strain response for the 3D fiber microstructure.

fSAM algorithm is considered to be converged in case no fiber-overlap is detected, the relative error of the fiber orientation tensor is below $\epsilon_{\mathbb{A}} = 10^{-4}$ and the relative error of the maximum curvature constraint drops below $\epsilon_{\bar{\kappa}} = 10^{-3}$.

We load the structure with the macroscopic normal strain $\bar{\varepsilon}_{22} = 3\,\%$ via periodic boundary conditions in $n_{\Delta t}$ loading steps. The time-step count, the necessary resolution and the required cell size for representativity are studied in the following investigations. Generated microstructures resolved a coarse and a fine mesh-size are shown in Fig. 11.

Study on the time-step size

The goal of this section is to select a sufficiently fine time-step size. Therefore, we consider a microstructure with cubic cell dimensions $Q_i = 420\,\mu\text{m}$ $(i = 1, 2, 3)$. The generated microstructure is resolved with a voxel-edge length $h = 1.25\,\mu\text{m}$. We study the time-step counts $n_{\Delta t} = 20$, 40, 80, 160, i.e., the time increments are $\Delta t = 0.15\,\text{s}$, $0.075\,\text{s}$, $0.0375\,\text{s}$ and $0.01875\,\text{s}$.

In Fig. 12(a), the computed effective stress-strain responses for the applied time-step counts are shown. We observe that the time increment significantly influences the computed material behavior. However, for increasing time-step count, convergence is obtained. Evaluating the absolute relative difference between the temporal resolutions at $\bar{\varepsilon}_{22} = 3\,\%$ compared to the smallest time increment,

we obtain errors of 21.33%, 9.11% and 2.98% for increasing time-step count. To obtain an error below 3%, we choose a time-step count of $n_{\Delta t} = 80$ for the following investigations.

Study on the resolution

A critical aspect of FFT-based homogenization is the spatial resolution of the input microstructure, which directly influences the accuracy of the computed effective properties. Insufficient resolution may fail to capture essential microscale features, while an excessively fine discretization can lead to high computational costs without significant gains in accuracy. The aim of this resolution study is to investigate the impact of the voxel resolution on the homogenized material properties. By evaluating the convergence behavior of the effective stress-strain behavior with increasing resolution, we seek to identify a suitable discretization level that ensures a reliable balance between computational efficiency and numerical accuracy.

We investigate the voxel-edge lengths $h = 1.0\,\mu\text{m}$, $1.25\,\mu\text{m}$, $2.0\,\mu\text{m}$ and $4.0\,\mu\text{m}$, which resolve the fiber diameter with 10, 8, 5 and 2.5 voxels. For the cubic cell dimensions, we select $Q_i = 420\,\mu\text{m}$. Thus, the microstructure is resolved with 105^3, i.e., about $1.2 \cdot 10^6$, voxels for the coarsest resolution and 420^3, i.e., about $74 \cdot 10^6$, voxels for the finest resolution. Due to the significantly increased number of voxels, the computational effort required to homogenize the finely resolved structure is substantially higher. The considered microstructure resolved with the coarsest and the finest mesh-size are shown in Fig. 11.

The computed effective stress-strain behavior is shown in Fig. 12(b). Due to the convexity and coercivity of the OT damage model, convergence for decreasing mesh-size is obtained. Evaluating the maximum relative resolution error of the stress-strain curves compared to the finest resolution reveals an error of 9.00% for the coarsest resolution, dropping to 3.32% and 1.40% with increasing voxel count. We require a resolution error below 3% and thus choose a voxel-edge length of $h = 1.25\,\mu\text{m}$, which is in accordance with previous studies on long fiber reinforced composites applying a purely elastic material model to the matrix material [105,106].

RVE study

Understanding the effective behavior of heterogeneous materials at the macroscopic level typically relies on detailed simulations of their microscopic structure. Instead of modeling the entire complexity of a material, computational homogenization uses simplified, smaller-scale models – so-called unit cells – to estimate global properties. A key challenge is ensuring that these unit cells are representative, i.e., that they capture the essential statistical and structural features of the material well enough to enable reliable macroscopic predictions.

In reality, the microstructure introduces randomness, so *apparent* material properties derived from finite unit cells vary across different configurations. As the cell size increases, this variability diminishes, and the results stabilize, approaching the so-called effective properties [54,55,110]. If a unit cell becomes large enough that further increases no longer affect the computed averages significantly, it is considered a *representative volume element* (RVE). In context of damage modeling with softening phenomena, the apparent properties will only converge to the effective properties if the material behavior is mesh-independent [56]. Thus, localization and the concept of representativity are incompatible.

Choosing the smallest possible RVE is the key to minimizing computational cost without sacrificing accuracy. One way to decrease the required unit cell size for representativity is through the use of periodic boundary conditions [111,112] and carefully controlled statistical descriptors, such as the fiber volume fraction or high-order orientation tensors, when generating synthetic microstructures [106,113].

To assess whether a unit cell is representative, we need to monitor two types of errors: the *random* and the *systematic* error [55,114]. The random error (or dispersion) refers to the variance in the apparent properties across different realizations of a microstructure at fixed cell size and typically vanishes as the domain grows. The systematic error (or bias), on the other hand, measures the discrepancy between the average apparent properties for a fixed unit cell size and the (generally unknown) effective properties. Since the effective properties are rarely available, convergence is evaluated by comparing the mean apparent properties for increasing cell-sizes.

In this RVE study, we consider the three unit cell sizes $Q_i = 280\,\mu\text{m}$, $420\,\mu\text{m}$ and $560\,\mu\text{m}$, and use the resolution $h = 1.25\,\mu\text{m}$. Thus, the smallest unit cell is resolved with 224^3, i.e., about $11 \cdot 10^6$, voxels and the largest unit cell with 448^3, i.e., about $90 \cdot 10^6$, voxels. To assess the representativity of the unit cells, we first generate ten microstructures for each unit cell size, and compute the stress-strain behavior for all generated microstructures. Subsequently, we evaluate the mean and the standard deviation of the stress σ_{22} for each unit cell size with respect to its ten realizations. Last but not least, we compute the relative error of the mean stress compared to the largest unit cell size

$$\delta\overline{\sigma}_{22} = \left| \frac{\text{mean}\left(\bar{\sigma}_{22,Q_i}\right) - \text{mean}\left(\bar{\sigma}_{22,560}\right)}{\text{mean}\left(\bar{\sigma}_{22,560}\right)} \right| \cdot 100\% \tag{4.17}$$

to assess the systematic error and the relative standard deviation

$$\text{RSD} = \frac{\text{std}\left(\bar{\sigma}_{22,Q_i}\right)}{\left|\text{mean}\left(\bar{\sigma}_{22,Q_i}\right)\right|} \cdot 100\% \tag{4.18}$$

to quantify the random error.

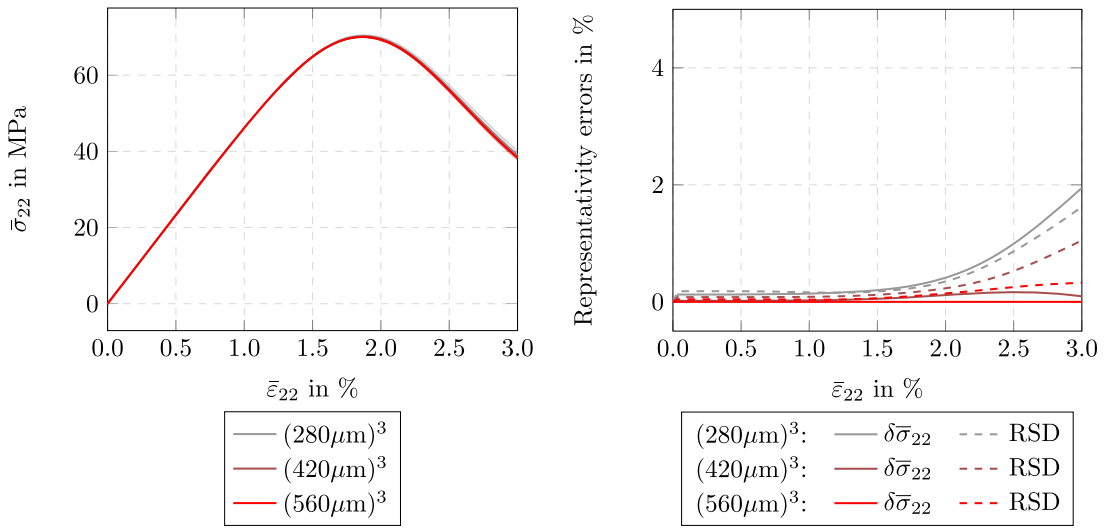

(a) Mean stress-strain curve with the scatter band

(b) Representativity errors

Fig. 13. On the influence of the unit-cell size for the 3D fiber ensemble.

The mean computed stress-strain curves with the resulting scatter bands are plotted in Fig. 13(a) for all unit cell sizes. We observe that distinguishing between the different curves is barely possible as the curves are in a close range. For a better overview of the differences, we have a look at the representativity errors in Fig. 13(b). It turns out that the random and the systematic are increasing along the loading path, but always are below 2%, proving the representativity of all unit cells. Hence, we emphasize that the OT damage model is applicable in the context of homogenization, ensuring moderate necessary resolutions and unit cell sizes for representativity. Such properties are crucial to predict the mechanical behavior in a reliable and efficient manner.

4.5. Matrix-failure mechanisms of unidirectional fiber reinforced composites

Last but not least, we investigate the matrix failure of unidirectional fiber-reinforced composites to identify the damage mechanisms predicted by our model. We generate short fiber reinforced microstructures with cubic cell dimensions of $Q_i = 280\mu m$ by the SAM algorithm [113,115], prescribing a fiber alignment in $\boldsymbol{e}_1$-direction, a uniform fiber length of $L = 100\,\mu m$, a fiber diameter of $D = 10\,\mu m$ and a fiber volume fraction of $\phi = 20\,\%$. According to the resolution study in Section 4.2, we resolve the microstructure with the voxel edge-length $h = 1.25\,\mu m$. A generated microstructure is shown in Fig. 14(a). The matrix and the fibers are modeled with the isotropic material parameters listed in Table 1, and we use the damage parameters $r = 1.00\,MPa$ and $\dot{d}_{max} = 4.00\,s^{-1}$ for the matrix material.

In three loading cases, we investigate the failure mechanisms of the matrix and plot the effective degradation fields in Fig. 14(b)–(d). For the first and the second loading case, we apply macroscopic normal strains in fiber direction ($\bar{\varepsilon}_{11} = 3\,\%$) and perpendicular to the fiber direction ($\bar{\varepsilon}_{22} = 3\,\%$), respectively. In the last scenario, we load the structure with macroscopic shear strain in fiber direction ($\bar{\varepsilon}_{12} = 3\,\%$). For all scenarios, we apply the load in 80 time steps with a total loading time of 3 s, imposing periodic boundary conditions.

For normal extension in fiber direction, the damage initiates at the fiber ends due to stress concentrations and evolves with increasing applied strain perpendicular to the loading direction. Thus, the loading condition evokes damage peaks at the end of the fibers in the loading direction, see Fig. 14(b), weakening the load transfer between the matrix and the fibers. In addition, we observe inter-fiber failure in the $\boldsymbol{e}_2 - \boldsymbol{e_3}$-plane as a result of the dilatation. The random arrangement of the fibers deflects the damage path as the damage grows between the fiber ends, preventing a strict propagation perpendicular to the loading directions. Applying the macroscopic normal strain $\bar{\varepsilon}_{22}$ perpendicular to the fiber direction leads to a damage evolution of the matrix in the $\boldsymbol{e}_1 - \boldsymbol{e_3}$-plane, as shown in Fig. 14(c), starting along the fiber boundaries. Hence, in contrast to the first loading scenario, the interfacial area between the matrix and the fibers is reduced along the edges of the fibers rather than at the end of the fibers. The effective degradation field associated to the shear loading in fiber direction 14(d) reveals similar damage mechanisms as for the normal tension perpendicular to the fiber axis, i.e., damage propagation in the $\boldsymbol{e}_1 - \boldsymbol{e_3}$-plane. The matrix-failure modes identified in this study are in agreement with previous investigations in the literature [116–119], indicating the validity of the damage prediction for the matrix in fiber-reinforced composites.

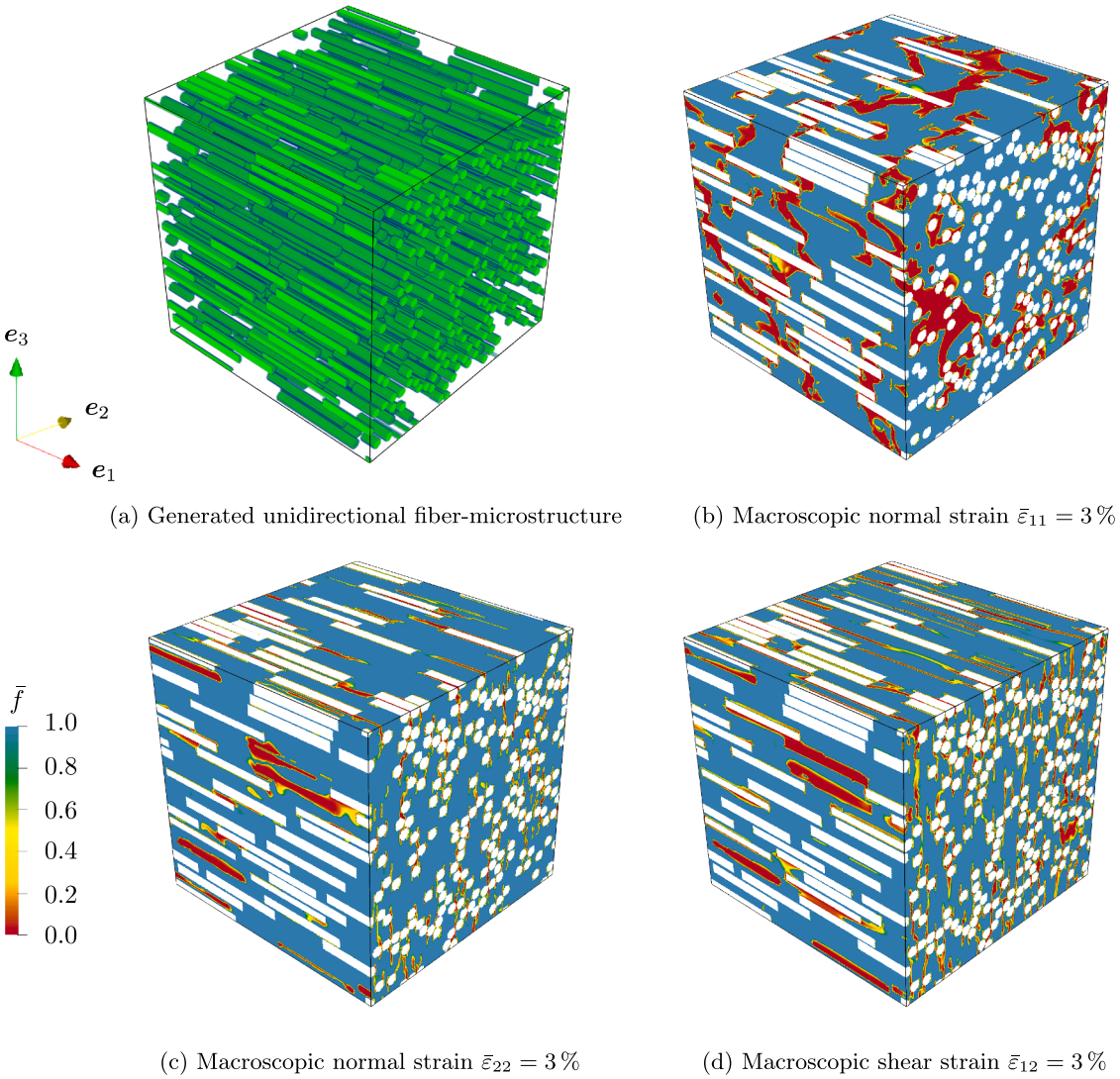

(a) Generated unidirectional fiber-microstructure

(b) Macroscopic normal strain $\bar{\varepsilon}_{11} = 3\,\%$

(c) Macroscopic normal strain $\bar{\varepsilon}_{22} = 3\,\%$

(d) Macroscopic shear strain $\bar{\varepsilon}_{12} = 3\,\%$

Fig. 14. Fiber-reinforced composite with unidirectional fiber arrangement (a) and the distribution of the effective degradation for three different loading conditions (b) - (d).

5. Conclusion

The goal of the work at hand was to complete the agenda of Schwarz et al. [59]: compute the convex envelope of the incremental condensed energy arising from a class of isotropic damage models with rate limitation. These developments were driven by the desire to simulate the stiffness degradation of a material exhibiting strain softening behavior within a component undergoing mechanical loading in a robust and mesh-independent way. To be more precise, our contributions include:

1. We identified a condition on the damage-degradation function which permits to compute the convex envelope explicitly: convexity of the reciprocal degradation function. Such a condition is quite natural due to the emergence of the harmonic mean in the degradation pre-factor in front of the undamaged elastic energy. Moreover, the condition is satisfied for the degradation functions considered in this manuscript: the exponential degradation as well as the elementary monomial degradation functions. It might be interesting to investigate other degradation functions like the ones reported by Wu and Nguyen [81].
2. We computed the convex envelope of the incremental time-discretized energy explicitly. We used a continuum formulation to handle all time steps in the same framework. It turned out that the optimal states arise as convex combinations of the extreme reachable damage states per load step: the undamaged state and the maximum damage reachable in this step. Interestingly, the compliance form of Hooke's elastic energy emerges naturally, which is convex in the strain and the compliance tensor [22] and was previously used ad-hoc in phenomenological damage models [120–122]. The devised model turns out to be convex in

a natural way – which is evident from its formulation(s) in terms of a generalized standard material with convex free energy. However, the space of internal (damage) variables is inherently infinite-dimensional. As the damage-distribution function point of view leads to more ambiguities than necessary, we also introduced another formulation based on measure theory and optimal transportation [74,93], a topic which is well-studied in mathematics but does not appear to be standard in continuum mechanical models.

3. Our findings also shed light on the model structure: Whereas classical phenomenological continuum-damage models use damage variables as arguments, the convexified model involves a probability distribution of a damage variable. This finding was already envisioned by Schwarz et al. [59] in their use of the "emulated RVE". The latter may be imagined as a one-dimensional rod with a distribution of Young's moduli, spread according to the damage distribution under consideration. The "effective" Young's modulus then arises from a harmonic average - a fact which is well-known in micromechanics and thermodynamics, corresponding to the Maxwell construction. Aside from this statics point-of-view, the dynamics of the entire damage evolution also emerges from the stepwise convexification procedure of the condensed incremental potential. As a result, the convexified local, i.e., gradient-free, damage model is able to reproduce a softening behavior because the localization takes place in "damage space", i.e., in the rod, and not in physical space.
4. Aside from the theoretical findings we introduced a full computational procedure to resolve the ensuing mechanical model: we discussed a natural time discretization for equidistant time steps in terms of convex combinations Dirac measures, i.e., *discrete damage distributions*, and provided a Newton-type method which permits to resolve the nonlinear systems arising for each time steps in a robust and efficient manner.
5. We provided an analysis of the properties of the resulting damage model. The convexity and the thermodynamical consistency of the model are more or less straightforward: the original (non-convex) damage model was formulated as a GSM, and the convexification procedure retains thermodynamical consistency - both the free energy and the dissipation distance are convex. Moreover, the fact that a convexification process leads to a convex model is not surprising. What is a bit more subtle is the lack of strict convexity of the resulting relaxed model: both the full energy (for the strain *and* the internal variables) and the condensed incremental energy (for the strain tensor only) lack strict convexity, in general. As a result, we cannot conclude uniqueness neither for the evolution of the internal variables nor the attained strain state per load increment. In hindsight, this fact is not surprising due to the linear dissipation distance of the original model and the emergence of the harmonic mean upon convex relaxation. An intriguing question here is whether the lack of strict convexity is a bug or a feature. Maybe the lack of uniqueness reflects the inherent stochasticity of the damage process.
6. We wish to stress the consequences of the salient properties of the convexified damage model: For a start, the convexity of the condensed incremental energy permits, together with suitable growth conditions, ensure the existence of minimizers to the associated mechanical boundary-value problems. Thus, no spurious mesh-dependence of the model is observed. In particular, as every local minimizer of a convex objective function is actually a global minimizer, certain pathological situations encountered for non-convex damage models are avoided. Moreover, convexity of the model permits *homogenization* to be simple: Periodic homogenization applies to such convex models, and the emerging homogenized materials involve single-cell formulas only, see Braides [123] and Müller [124], avoiding multi-cell homogenization formulas required for non-convex energies. Moreover, other issues observed for non-convex models, like the fact that homogenization and letting the time-step size go to zero do not commute as limiting procedures, see the relevant works [125–127], are not expected to occur. Whether these advantageous properties actually reflect the underlying physics is another matter, however.
7. Last but not least we provided pertinent computational examples, showing the performance and robustness of the convexified model and its computational realization, both on material-point level and within a homogenization setting. Due to the salient features of the convexified damage model, it may be used in dedicated upscaling schemes [128–130] to predict the material degradation including softening effects of components made of microstructured materials.

Apart from the contributions, we also list a number of loose ends and interesting questions to ponder.

1. The manuscript at hand was limited to convexifying a *linear-elastic* isotropic damage model without tension-compression anisotropy. Lifting each of these constraints would be interesting: Dealing with anisotropic damage, incorporating tension-compression asymmetry or extending the framework to inelastic material models like plasticity or viscoelasticity could prove fruitful, in particular when using the obtained model(s) for representing practical materials beyond the theoretical setting of the article at hand.
2. There is a number of mathematical questions that might be of interest. We performed relaxation *after* time discretization. Letting the time-step size go to zero might shed further light onto the model. Moreover, it would be interesting to find out whether strict convexity could be introduced into the model. Presumably, this is possible in a variety of ways, and the ramification should be studied. Last but not least, it might be interesting to find out whether rate-independence can be realized in this framework as envisioned by Schwarz et al. [59].
3. From the point of view of computational mechanics it is desirable to study which discretization schemes to use. For a start, we used equidistant time steps only, and monitored discrete damage distributions. Such a naive procedure does not appear optimal, in particular when non-equidistant time steps are used. Moreover, it might be worthwhile to study if fully continuous schemes may be used. Here, a transfer from the optimal transport literature [131] might be advised.
4. The derived convexified model behaves strongly like the model envisioned by Schwarz et al. [59], which is conceptually much simpler. It might be useful to study the connections more closely, e.g., finding conditions under which both models behave similarly.

5. The investigated model [59] involves the abstract parameters r and $d_{\max}$. It would be desirable to establish the connection to experimentally measurable quantities such as the fracture energy or the critical strain energy density.
6. This work was concerned with the mathematical details required to set up a continuum damage model that is local and permits to represent a softening behavior without spurious mesh dependence of the finite-element results. With this focus, less effort was spent on discussing the potential applications of the resulting model, e.g., to damage prediction in polymers, quasi-brittle materials or structural composites.

CRediT authorship contribution statement

Celine Lauff: Conceptualization, Methodology, Software, Validation, Formal analysis, Investigation, Data curation, Writing – original draft, Writing – review & editing, Visualization, Project administration; **Matti Schneider:** Conceptualization, Methodology, Software, Formal analysis, Resources, Writing – original draft, Writing – review & editing, Supervision, Project administration, Funding acquisition; **Thomas Böhlke:** Resources, Writing – review & editing, Supervision, Project administration, Funding acquisition.

Data availability

Data will be made available on request.

Declaration of competing interest

The authors declare that they have no known competing financial interests or personal relationships that could have appeared to influence the work reported in this paper.

Acknowledgment

Matti Schneider acknowledges the support from the European Research Council within the Horizon Europe program - project 101040238. Celine Lauff and Thomas Böhlke acknowledge the partial support by the German Research Foundation (DFG) within the International Research Training Group “Integrated engineering of continuous-discontinuous long fiber reinforced polymer structures” (GRK 2078) – project 255730231. We are grateful to Johannes Gisy (KIT, Institute of Engineering Mechanics) for providing constructive feedback to an early version of the manuscript. We thank the anonymous reviewers for their insightful comments and valuable suggestions which led to improvements of the manuscript.

Appendix A. The emergence of the harmonic mean

The goal of this section is to provide arguments for the validity of the identity (2.38)

$$\min_{\langle\boldsymbol{\varepsilon}\rangle_{[0,1]}=\bar{\boldsymbol{\varepsilon}}} \left\langle \frac{f(d)}{2}\,\boldsymbol{\varepsilon}\cdot\mathbb{C}[\boldsymbol{\varepsilon}] \right\rangle_{[0,1]} = \frac{\bar{f}(d)}{2}\,\bar{\boldsymbol{\varepsilon}}\cdot\mathbb{C}[\bar{\boldsymbol{\varepsilon}}]. \tag{A.1}$$

For this purpose, we re-write the optimization problem on the left-hand side in Lagrangian form

$$\left\langle \frac{f(d)}{2}\,\boldsymbol{\varepsilon}\cdot\mathbb{C}[\boldsymbol{\varepsilon}] \right\rangle_{[0,1]} + \boldsymbol{\Lambda}\cdot\left(\langle\boldsymbol{\varepsilon}\rangle_{[0,1]}-\bar{\boldsymbol{\varepsilon}}\right) \longrightarrow \min_{\boldsymbol{\varepsilon}}\max_{\boldsymbol{\Lambda}}, \tag{A.2}$$

with a Lagrangian multiplier $\boldsymbol{\Lambda}\in\mathrm{Sym}(n)$. The Karush-Kuhn-Tucker (KKT) conditions compute as

$$f(d)\,\mathbb{C}[\boldsymbol{\varepsilon}] + \boldsymbol{\Lambda} = \mathbf{0}, \tag{A.3}$$

$$\langle\boldsymbol{\varepsilon}\rangle_{[0,1]} - \bar{\boldsymbol{\varepsilon}} = \mathbf{0}. \tag{A.4}$$

Solving the first equation explicitly for the strain field $\boldsymbol{\varepsilon}$,

$$\boldsymbol{\varepsilon} = -f(d)^{-1}\mathbb{C}^{-1}\cdot\boldsymbol{\Lambda}, \tag{A.5}$$

averaging yields the equation

$$\langle\boldsymbol{\varepsilon}\rangle_{[0,1]} = -\left\langle f(d)^{-1}\right\rangle_{[0,1]}\mathbb{C}^{-1}\cdot\boldsymbol{\Lambda}. \tag{A.6}$$

Inserting this insight into the second Eq. (A.4)

$$\bar{\boldsymbol{\varepsilon}} = -\left\langle f(d)^{-1}\right\rangle_{[0,1]}\mathbb{C}^{-1}\cdot\boldsymbol{\Lambda} \tag{A.7}$$

provides an explicit expression of the Lagrange multiplier

$$\boldsymbol{\Lambda} = -\left\langle f(d)^{-1}\right\rangle_{[0,1]}^{-1}\mathbb{C}[\bar{\boldsymbol{\varepsilon}}]. \tag{A.8}$$

In particular, we arrive at the following formula for the local strain

$$\boldsymbol{\varepsilon} = f(d)^{-1}\left\langle f(d)^{-1}\right\rangle_{[0,1]}^{-1}\bar{\boldsymbol{\varepsilon}}. \tag{A.9}$$

With this result at hand, the desired identity (A.1) follows readily, as we observe

$$\begin{aligned}\left\langle \frac{f(d)}{2}\,\boldsymbol{\varepsilon}\cdot\mathbb{C}[\boldsymbol{\varepsilon}]\right\rangle_{[0,1]} &= \left\langle \frac{f(d)}{2}\left(f(d)^{-1}\left\langle f(d)^{-1}\right\rangle_{[0,1]}^{-1}\bar{\boldsymbol{\varepsilon}}\right)\cdot\mathbb{C}\left[f(d)^{-1}\left\langle f(d)^{-1}\right\rangle_{[0,1]}^{-1}\bar{\boldsymbol{\varepsilon}}\right]\right\rangle_{[0,1]}\\ &= \frac{1}{2}\left\langle f(d)\,f(d)^{-2}\right\rangle_{[0,1]}\left\langle f(d)^{-1}\right\rangle_{[0,1]}^{-2}\bar{\boldsymbol{\varepsilon}}\cdot\mathbb{C}[\bar{\boldsymbol{\varepsilon}}]\\ &= \frac{1}{2}\left\langle f(d)^{-1}\right\rangle_{[0,1]}^{-1}\bar{\boldsymbol{\varepsilon}}\cdot\mathbb{C}[\bar{\boldsymbol{\varepsilon}}].\end{aligned} \tag{A.10}$$

Appendix B. Mathematical details for the mixing formula (2.41)

The purpose of this section is to show that the quantities (2.35)

$$\psi^c_{\mathrm{cond}}(\bar{\boldsymbol{\varepsilon}}) = \min\left\{\bar{f}(d)\,\psi_0(\bar{\boldsymbol{\varepsilon}}) + r\,\langle d-d^-\rangle_{[0,1]}\,\middle|\, d^-\le d\le d^+\right\} \tag{B.1}$$

and (2.41)

$$\tilde{\psi}^c_{\mathrm{cond}}(\bar{\boldsymbol{\varepsilon}}) = \min_{\phi:[0,1]\to[0,1]}\left\langle (1-\phi)f(d^-)^{-1} + \phi\, f\left(d^+\right)^{-1}\right\rangle^{-1}_{[0,1]}\psi_0(\bar{\boldsymbol{\varepsilon}}) + r\left\langle \phi\left(d^+-d^-\right)\right\rangle_{[0,1]} \tag{B.2}$$

coincide for given piece-wise constant functions $d^\pm:[0,1]\to[d,d_{\max})$ which we assume to satisfy the inequalities $d^-\le d^+$ point-wise. We will follow a sandwich strategy, i.e., we will show that both inequalities

$$\psi^c_{\mathrm{cond}}(\bar{\boldsymbol{\varepsilon}})\le\tilde{\psi}^c_{\mathrm{cond}}(\bar{\boldsymbol{\varepsilon}}) \quad\text{and}\quad \tilde{\psi}^c_{\mathrm{cond}}(\bar{\boldsymbol{\varepsilon}})\le\psi^c_{\mathrm{cond}}(\bar{\boldsymbol{\varepsilon}}) \tag{B.3}$$

hold for every strain $\bar{\boldsymbol{\varepsilon}}\in\mathrm{Sym}(n)$, leading to the desired equality of the expressions (B.1) and (B.2)
We start with the"simple" case $\psi^c_{\mathrm{cond}}(\bar{\boldsymbol{\varepsilon}})\le\tilde{\psi}^c_{\mathrm{cond}}(\bar{\boldsymbol{\varepsilon}})$. We assumed that the lower and upper bound functions d^- and d^+ are piece-wise constant, i.e., there is a decomposition of the interval $[0,1]$ into K disjoint intervals I_a $(a=1,2,\dots,K)$ on which the functions d^- and d^+ take constant values $d^\pm_a$ $(a=1,2,\dots,K)$. Let $\phi:[0,1]\to[0,1]$ be fixed. We will construct a function $d:[0,1]\to\mathbb{R}_{\ge0}$ which satisfies the constraints $d^-\le d\le d^+$ point-wise, together with the equality

$$\bar{f}(d)\,\psi_0(\bar{\boldsymbol{\varepsilon}}) + r\,\langle d-d^-\rangle_{[0,1]} = \left\langle (1-\phi)f(d^-)^{-1} + \phi\, f\left(d^+\right)^{-1}\right\rangle^{-1}_{[0,1]}\psi_0(\bar{\boldsymbol{\varepsilon}}) + r\left\langle \phi\left(d^+-d^-\right)\right\rangle_{[0,1]}. \tag{B.4}$$

Thus, as the left-hand side of Eq. (B.4) is greater or equal than the minimum, we deduce the estimate

$$\psi^c_{\mathrm{cond}}(\bar{\boldsymbol{\varepsilon}})\le\left\langle (1-\phi)f(d^-)^{-1} + \phi\, f\left(d^+\right)^{-1}\right\rangle^{-1}_{[0,1]}\psi_0(\bar{\boldsymbol{\varepsilon}}) + r\left\langle \phi\left(d^+-d^-\right)\right\rangle_{[0,1]}. \tag{B.5}$$

Minimizing the right-hand side w.r.t. $\phi:[0,1]\to[0,1]$ then yields the desired inequality $\psi^c_{\mathrm{cond}}(\bar{\boldsymbol{\varepsilon}})\le\tilde{\psi}^c_{\mathrm{cond}}(\bar{\boldsymbol{\varepsilon}})$. Thus, for this direction, it remains to construct the function d following the prescribed field ϕ. In view of the decomposition $\{I_a\}_{a=1}^K$, we observe

$$\begin{aligned}\left\langle (1-\phi)f(d^-)^{-1} + \phi\, f\left(d^+\right)^{-1}\right\rangle_{[0,1]} &= \sum_{a=1}^K\int_{I_a}(1-\phi(s))f\left(d^-_a\right)^{-1} + \phi(s)\,f\left(d^+_a\right)^{-1}\,\mathrm{d}s\\ &= \sum_{a=1}^K\left((1-\phi_a)f\left(d^-_a\right)^{-1} + \phi_a\,f\left(d^+_a\right)^{-1}\right)\int_{I_a}\mathrm{d}s\end{aligned} \tag{B.6}$$

with the means

$$\phi_a = \int_{I_a}\phi(s)\,\mathrm{d}s\Big/\int_{I_a}\mathrm{d}s\in[0,1]. \tag{B.7}$$

Similarly, it holds

$$\left\langle \phi\left(d^+-d^-\right)\right\rangle_{[0,1]} = \sum_{a=1}^K\phi_a\left(d^+_a-d^-_a\right)\int_{I_a}\mathrm{d}s. \tag{B.8}$$

Then, the function d is constructed as follows: It takes the value d^-_a on the left $(1-\phi_a)$-portion of the interval I_a, and is defined to be d^+_a on the remainder of the interval. Then, it is readily checked that the identities

$$\left\langle f(d)^{-1}\right\rangle_{[0,1]} = \sum_{a=1}^K\left((1-\phi_a)f\left(d^-_a\right)^{-1} + \phi_a\,f\left(d^+_a\right)^{-1}\right)\int_{I_a}\mathrm{d}s \tag{B.9}$$

and

$$\langle d-d^-\rangle_{[0,1]} = \sum_{a=1}^K\phi_a\left(d^+_a-d^-_a\right)\int_{I_a}\mathrm{d}s \tag{B.10}$$

hold. In particular, the identity (B.4) is seen to be true.
The remainder of this section is devoted to establishing the validity of the converse inequality (B.3) $\tilde{\psi}^{c}_{\mathrm{cond}}(\bar{\varepsilon}) \leq \psi^{c}_{\mathrm{cond}}(\bar{\varepsilon})$. To proceed, we fix a damage field

$$d : [0,1] \to \mathbb{R}_{\geq 0} \quad \text{which respects the constraints} \quad d^- \leq d \leq d^+. \tag{B.11}$$

We will construct a field $\phi : [0,1] \to [0,1]$, s.t. the inequality

$$\Big\langle (1-\phi) f(d^-)^{-1} + \phi\, f\big(d^+\big)^{-1} \Big\rangle^{-1}_{[0,1]} \psi_0(\bar{\varepsilon}) + r\, \Big\langle \phi\big(d^+ - d^-\big) \Big\rangle_{[0,1]} \leq \bar{f}(d)\, \psi_0(\bar{\varepsilon}) + r\, \langle d - d^- \rangle_{[0,1]} \tag{B.12}$$

holds true. Minimizing the left-hand side and using the definition (B.2), we thus obtain the estimate

$$\tilde{\psi}^{c}_{\mathrm{cond}}(\bar{\varepsilon}) \leq \bar{f}(d)\, \psi_0(\bar{\varepsilon}) + r\, \langle d - d^- \rangle_{[0,1]}. \tag{B.13}$$

Then, minimizing with respect to the admissible damage fields (B.1), we are led to the desired estimate $\tilde{\psi}^{c}_{\mathrm{cond}}(\bar{\varepsilon}) \leq \psi^{c}_{\mathrm{cond}}(\bar{\varepsilon})$.
So, it remains to construct the field ϕ and establish the estimate (B.12). Actually, we select the field ϕ point-wise, so that the identity

$$d(s) = (1-\phi(s))\, d^-(s) + \phi(s)\, d^+(s), \quad s \in [0,1], \tag{B.14}$$

is satisfied. Here, we use that the damage field d satisfies the constraints (B.11), s.t. each value may be represented as a convex combination (B.14). Due to the assumed convexity of the function (2.39), we are led to the inequality

$$g(d(s)) \equiv g\big((1-\phi(s))\, d^-(s) + \phi(s)\, d^+(s)\big) \leq (1-\phi(s))\, g(d^-(s)) + \phi(s)\, g\big(d^+(s)\big). \tag{B.15}$$

Averaging yields the estimate

$$\langle g(d) \rangle_{[0,1]} \leq \Big\langle (1-\phi)\, g(d^-) + \phi\, g(d^+) \Big\rangle_{[0,1]}, \tag{B.16}$$

or, rather, by taking inverses

$$\Big\langle (1-\phi)\, f(d^-)^{-1} + \phi\, f\big(d^+\big)^{-1} \Big\rangle^{-1}_{[0,1]} \leq \big\langle f(d)^{-1} \big\rangle^{-1}_{[0,1]} \equiv \bar{f}(d), \tag{B.17}$$

As the factor $\psi_0(\bar{\varepsilon})$ is non-negative, we are led to the estimate

$$\Big\langle (1-\phi)\, f(d^-)^{-1} + \phi\, f\big(d^+\big)^{-1} \Big\rangle^{-1}_{[0,1]} \psi_0(\bar{\varepsilon}) \leq \bar{f}(d)\, \psi_0(\bar{\varepsilon}). \tag{B.18}$$

Due to the definition (B.14), we notice

$$\begin{aligned} \langle d - d^- \rangle_{[0,1]} &= \big\langle (1-\phi)\, d^- + \phi\, d^+ - d^- \big\rangle_{[0,1]} \\ &= \big\langle -\phi\, d^- + \phi\, d^+ \big\rangle_{[0,1]} \\ &= \big\langle \phi\, \big(d^+ - d^-\big) \big\rangle_{[0,1]}. \end{aligned} \tag{B.19}$$

In particular, multiplying by the positive factor r, the desired inequality (B.12)

$$\Big\langle (1-\phi)\, f(d^-)^{-1} + \phi\, f\big(d^+\big)^{-1} \Big\rangle^{-1}_{[0,1]} \psi_0(\bar{\varepsilon}) + r \big\langle \phi\, \big(d^+ - d^-\big) \big\rangle_{[0,1]} \leq \bar{f}(d)\, \psi_0(\bar{\varepsilon}) + r \langle d - d^- \rangle_{[0,1]} \tag{B.20}$$

emerges.

Appendix C. Arguments for the convexity properties of the condensed incremental energy

C.1. Two-sided quadratic bounds

The purpose of this Appendix is to provide arguments for the validity of property (i) listed in Section 3.3, i.e., the existence of positive constants α_-, α_+ and C_+, s.t. the bounds (3.33)

$$\frac{\alpha_-}{2}\, \varepsilon \cdot \mathbb{C}[\varepsilon] \leq \psi_{\mathrm{cond}}(\varepsilon) \leq C_+ + \frac{\alpha_+}{2}\, \varepsilon \cdot \mathbb{C}[\varepsilon] \tag{C.1}$$

are valid for all strains $\varepsilon \in \mathrm{Sym}(n)$. To do so, we infer the definition of the factors g_j, see Eq. (3.8)

$$g_j = f(d_j)^{-1}, \quad j = 0, 1, \dots, N. \tag{C.2}$$

The considered degradation function f is assumed to be monotonically decreasing and the damage values d_j are increasing (3.4). Thus, by the relation (C.2), the estimates

$$f_0 \geq f_j \geq f_N, \quad j = 0, 1, \dots, N, \tag{C.3}$$

imply the two-sided bounds

$$g_0 \leq g_j \leq g_N, \quad j = 0, 1, \dots, N. \tag{C.4}$$

The simplex constraints (3.6)

$$\rho_j \geq 0 \quad (j = 0, 1, \dots, N) \quad \text{and} \quad \sum_{j=0}^{N} \rho_j = 1 \tag{C.5}$$

imply the estimate

$$g_N \leq \sum_{j=0}^{N} \rho_j \, g_j \leq g_0. \tag{C.6}$$

Consequently, we obtain the inequalities

$$\frac{1}{2g_0}\boldsymbol{\varepsilon} \cdot \mathbb{C}[\boldsymbol{\varepsilon}] \leq \left(\sum_{j=0}^{N} \rho_j(\boldsymbol{\Phi}) \, g_j \right)^{-1} \frac{1}{2} \, \boldsymbol{\varepsilon} \cdot \mathbb{C}[\boldsymbol{\varepsilon}] \leq \frac{1}{2g_N}\boldsymbol{\varepsilon} \cdot \mathbb{C}[\boldsymbol{\varepsilon}], \quad \forall \, \boldsymbol{\varepsilon} \in \mathrm{Sym}(n), \tag{C.7}$$

for the free energy. For the dissipation (3.12)

$$\mathcal{D}(\boldsymbol{\Phi}) = r \sum_{j=0}^{N-1} \rho_j^k \, \phi_j \, \Delta d_j \quad \text{with} \quad \Delta d_j = d_{j+1} - d_j > 0, \tag{C.8}$$

the bounds

$$0 \leq r \sum_{j=0}^{N-1} \rho_j^k \, \phi_j \, \Delta d_j \leq r \sum_{j=0}^{N-1} \rho_j^k \, \Delta d_j \tag{C.9}$$

are immediate in view of the box constraints $\phi_j \in [0, 1]$. By definition of the incremental energy (3.32)

$$P(\boldsymbol{\varepsilon}, \boldsymbol{\Phi}) = \left(\sum_{j=0}^{N} \rho_j(\boldsymbol{\Phi}) \, g_j \right)^{-1} \frac{1}{2} \, \boldsymbol{\varepsilon} \cdot \mathbb{C}[\boldsymbol{\varepsilon}] + r \sum_{j=0}^{N-1} \rho_j^k \, \phi_j \, \Delta d_j, \tag{C.10}$$

the estimates (C.7) and (C.9) imply the bound

$$\frac{1}{2g_0}\boldsymbol{\varepsilon} \cdot \mathbb{C}[\boldsymbol{\varepsilon}] \leq P(\boldsymbol{\varepsilon}, \boldsymbol{\Phi}) \leq \frac{1}{2g_N}\boldsymbol{\varepsilon} \cdot \mathbb{C}[\boldsymbol{\varepsilon}] + r \sum_{j=0}^{N-1} \rho_j^k \, \Delta d_j, \quad \forall \, \boldsymbol{\varepsilon} \in \mathrm{Sym}(n). \tag{C.11}$$

As the derived bounds are independent of the variable $\boldsymbol{\Phi}$ to be optimized, minimization w.r.t. $\boldsymbol{\Phi} \in [0, 1]^N$ leads to the desired bounds (C.1) with the constants

$$\alpha_- = \frac{1}{g_0}, \quad \alpha_+ = \frac{1}{g_N} \quad \text{and} \quad C_+ = r \sum_{j=0}^{N-1} \rho_j^k \, \Delta d_j. \tag{C.12}$$

C.2. Convexity of the condensed incremental energy

The purpose of this Appendix is to show that the condensed incremental energy (3.31)

$$\psi_{\mathrm{cond}}(\boldsymbol{\varepsilon}) := \min_{\boldsymbol{\Phi} \in [0,1]^N} P(\boldsymbol{\varepsilon}, \boldsymbol{\Phi}), \quad \boldsymbol{\varepsilon} \in \mathrm{Sym}(n), \tag{C.13}$$

is a convex function of its argument. This (standard) fact follows directly from the convexity of the function P, see Eq. (2.50). We provide the argument for the convenience of the reader.
The condensed incremental energy (C.13) is convex provided the inequality

$$\psi_{\mathrm{cond}}(\lambda \, \boldsymbol{\varepsilon}_1 + (1 - \lambda) \, \boldsymbol{\varepsilon}_2) \leq \lambda \, \psi_{\mathrm{cond}}(\boldsymbol{\varepsilon}_1) + (1 - \lambda) \, \psi_{\mathrm{cond}}(\boldsymbol{\varepsilon}_2) \tag{C.14}$$

holds for all strains $\boldsymbol{\varepsilon}_1, \boldsymbol{\varepsilon}_2 \in \mathrm{Sym}(n)$ and all $\lambda \in [0, 1]$. For any two such strains, there are associated states $\boldsymbol{\Phi}_1, \boldsymbol{\Phi}_2 \in [0, 1]^N$ realizing the minimum (C.13), i.e., the equations

$$\psi_{\mathrm{cond}}(\boldsymbol{\varepsilon}_i) = P(\boldsymbol{\varepsilon}_i, \boldsymbol{\Phi}_i), \quad i = 1, 2, \tag{C.15}$$

are satisfied. By the convexity of the function P, the estimate

$$P(\lambda \, \boldsymbol{\varepsilon}_1 + (1 - \lambda) \, \boldsymbol{\varepsilon}_2, \lambda \, \boldsymbol{\Phi}_1 + (1 - \lambda) \, \boldsymbol{\Phi}_2) \leq \lambda \, P(\boldsymbol{\varepsilon}_1, \boldsymbol{\Phi}_1) + (1 - \lambda) \, P(\boldsymbol{\varepsilon}_2, \boldsymbol{\Phi}_2) \tag{C.16}$$

holds for all parameters $\lambda \in [0, 1]$. By definition (C.13), the left-hand side is not smaller than

$$\psi_{\mathrm{cond}}(\lambda \, \boldsymbol{\varepsilon}_1 + (1 - \lambda) \, \boldsymbol{\varepsilon}_2) \equiv \min_{\boldsymbol{\Phi} \in [0,1]^N} P\big(\lambda \, \boldsymbol{\varepsilon}_1 + (1 - \lambda) \, \boldsymbol{\varepsilon}_2, \boldsymbol{\Phi}\big) \leq P(\lambda \, \boldsymbol{\varepsilon}_1 + (1 - \lambda) \, \boldsymbol{\varepsilon}_2, \lambda \, \boldsymbol{\Phi}_1 + (1 - \lambda) \, \boldsymbol{\Phi}_2), \tag{C.17}$$

whereas the right-hand side may be re-written via the expressions (C.15). Thus, we obtain the desired inequality (C.14), finishing the argument.

C.3. Lack of strict convexity of the condensed incremental energy

The goal of this Appendix is to show that the condensed incremental energy (3.31)

$$\psi_{\text{cond}}(\boldsymbol{\varepsilon}) := \min_{\boldsymbol{\phi}\in[0,1]^N} P(\boldsymbol{\varepsilon}, \boldsymbol{\phi}), \quad \boldsymbol{\varepsilon} \in \text{Sym}(n), \tag{C.18}$$

is not strictly convex, in general. For this purpose, we consider the first time step (2.43) only, where the condensed incremental energy (3.32) reduces to the form

$$\psi_{\text{cond}}(\boldsymbol{\varepsilon}) := \min_{\phi\in[0,1]} \frac{\psi_0(\boldsymbol{\varepsilon})}{(1-\phi)\, g_0 + \phi\, g_1} + \phi\, r\,(d_1 - d_0), \quad \boldsymbol{\varepsilon} \in \text{Sym}(n), \tag{C.19}$$

with the undamaged elastic energy (2.17)

$$\psi_0(\boldsymbol{\varepsilon}) = \frac{1}{2}\, \boldsymbol{\varepsilon} \cdot \mathbb{C}[\boldsymbol{\varepsilon}], \quad \boldsymbol{\varepsilon} \in \text{Sym}(n). \tag{C.20}$$

To increase readability, we introduce specific notation for this appendix only, and write

$$d_- \equiv d_0, \quad d_+ \equiv d_1, \quad g_- = g_0, \quad g_+ = g_1. \tag{C.21}$$

Thus, the expression (C.19) becomes

$$\psi_{\text{cond}}(\boldsymbol{\varepsilon}) := \min_{\phi\in[0,1]} \frac{\psi_0(\boldsymbol{\varepsilon})}{(1-\phi)\, g_- + \phi\, g_+} + \phi\, r\,(d_+ - d_-), \quad \boldsymbol{\varepsilon} \in \text{Sym}(n). \tag{C.22}$$

The problem (C.22) is just a simple one-dimensional optimization problem, and the solution ϕ may be computed explicitly:

$$\phi = R_{[0,1]}\left(\frac{\sqrt{\dfrac{g_+ - g_-}{d_+ - d_-}\, \dfrac{\psi_0(\boldsymbol{\varepsilon})}{r}} - g_-}{g_+ - g_-} \right) \tag{C.23}$$

with the clipping function

$$R_{[0,1]} : \mathbb{R} \to [0,1], \quad x \mapsto \max(\min(x,1),0). \tag{C.24}$$

For strains $\boldsymbol{\varepsilon} \in \text{Sym}(n)$ with an undamaged elastic energy in the range

$$\psi_0(\boldsymbol{\varepsilon}) \in \left[r\, g_-^2\, \frac{d_+ - d_-}{g_+ - g_-}, r\, g_+^2\, \frac{d_+ - d_-}{g_+ - g_-} \right], \tag{C.25}$$

the associated volume fraction ϕ satisfies the equation

$$\psi_0(\boldsymbol{\varepsilon})\, \frac{g_+ - g_-}{((1-\phi)\, g_- + \phi\, g_+)^2} = r\,(d_+ - d_-), \tag{C.26}$$

which we may re-write in the form

$$(1-\phi)\, g_- + \phi\, g_+ = \sqrt{\frac{\psi_0(\boldsymbol{\varepsilon})}{r}\, \frac{g_+ - g_-}{d_+ - d_-}}. \tag{C.27}$$

Thus, in view of the definition (C.22) and the expressions (C.23) as well as (C.26) for strains in the range (C.25), we are led to the formula

$$\begin{aligned} \psi_{\text{cond}}(\boldsymbol{\varepsilon}) &= \frac{\psi_0(\boldsymbol{\varepsilon})}{\sqrt{\dfrac{\psi_0(\boldsymbol{\varepsilon})}{r}\, \dfrac{g_+ - g_-}{d_+ - d_-}}} + r\,(d_+ - d_-)\, \frac{\sqrt{\dfrac{g_+ - g_-}{d_+ - d_-}\, \dfrac{\psi_0(\boldsymbol{\varepsilon})}{r}} - g_-}{g_+ - g_-} \\ &= 2\sqrt{r\, \frac{d_+ - d_-}{g_+ - g_-}}\, \sqrt{\psi_0(\boldsymbol{\varepsilon})} - r\, g_-\, \frac{d_+ - d_-}{g_+ - g_-}, \end{aligned} \tag{C.28}$$

which we may also write in the more abstract form

$$\psi_{\text{cond}}(\boldsymbol{\varepsilon}) = A\, \sqrt{\psi_0(\boldsymbol{\varepsilon})} + B \tag{C.29}$$

for strains $\boldsymbol{\varepsilon} \in \text{Sym}(n)$ satisfying the constraints (C.25) with the constants

$$A = 2\sqrt{r\, \frac{d_+ - d_-}{g_+ - g_-}} \quad \text{and} \quad B = -r\, g_-\, \frac{d_+ - d_-}{g_+ - g_-}. \tag{C.30}$$

After these preliminaries, we announce our strategy for showing the lack of strict convexity of the condensed incremental energy (C.22): We pick two different strains ε_1 and ε_2 obeying the constraints (C.25) and show, with the help of the representation formula (C.29), that the condensed incremental energy (C.22) is precisely linear over the interpolated strains

$$\varepsilon(\lambda) = \lambda\,\varepsilon_1 + (1-\lambda)\,\varepsilon_2, \quad \lambda \in [0,1]. \tag{C.31}$$

In case of strict convexity, the values of the condensed incremental energy at interior interpolation points, $\lambda \in (0,1)$, would need to be strictly less than their linear interpolation:

$$\psi_{\mathrm{cond}}(\varepsilon(\lambda)) \overset{!}{<} \lambda\,\psi_{\mathrm{cond}}(\varepsilon_1) + (1-\lambda)\,\psi_{\mathrm{cond}}(\varepsilon_2), \quad 0<\lambda<1. \tag{C.32}$$

In particular, as soon as we show the identity

$$\psi_{\mathrm{cond}}(\varepsilon(\lambda)) = \lambda\,\psi_{\mathrm{cond}}(\varepsilon_1) + (1-\lambda)\,\psi_{\mathrm{cond}}(\varepsilon_2), \quad 0<\lambda<1, \tag{C.33}$$

strict convexity of the condensed incremental energy is ruled out.
We pick a strain $\varepsilon_1 \in \mathrm{Sym}(n)$ with elastic energy

$$\psi_0(\varepsilon_1) = r\,g_-^2\,\frac{d_+ - d_-}{g_+ - g_-}, \tag{C.34}$$

and consider the rescaled strain

$$\varepsilon_2 = M\,\varepsilon_1 \tag{C.35}$$

with a rescaling factor $M > 1$ that we choose in such a way that the equation

$$\psi_0(\varepsilon_2) = r\,g_+^2\,\frac{d_+ - d_-}{g_+ - g_-} \tag{C.36}$$

is satisfied, i.e., we set

$$M = \frac{g_+}{g_-}. \tag{C.37}$$

The strains are chosen to represent the boundary cases for the admissible range (C.25). As the elastic energy (C.20) scales quadratically, we observe

$$\psi_{\mathrm{cond}}(\varepsilon_1) = A\,\sqrt{\psi_0(\varepsilon_1)} + B, \tag{C.38}$$

$$\psi_{\mathrm{cond}}(\varepsilon_2) = A\,M\,\sqrt{\psi_0(\varepsilon_1)} + B, \tag{C.39}$$

$$\psi_{\mathrm{cond}}(\varepsilon(\lambda)) = A\,[\lambda + (1-\lambda)M]\sqrt{\psi_0(\varepsilon_1)} + B, \tag{C.40}$$

where we used the expression

$$\varepsilon(\lambda) = \lambda\,\varepsilon_1 + (1-\lambda)\,\varepsilon_2 = \lambda\,\varepsilon_1 + (1-\lambda)M\,\varepsilon_1 = [\lambda + (1-\lambda)M]\varepsilon_1. \tag{C.41}$$

In particular, we observe

$$\begin{aligned}
\psi_{\mathrm{cond}}(\varepsilon(\lambda)) &= A\,[\lambda + (1-\lambda)M]\sqrt{\psi_0(\varepsilon_1)} + B \\
&= A\,\lambda\,\sqrt{\psi_0(\varepsilon_1)} + (1-\lambda)\,A\,M\sqrt{\psi_0(\varepsilon_1)} + B \\
&= \lambda\Big(A\,\sqrt{\psi_0(\varepsilon_1)} + B\Big) + (1-\lambda)\Big(A\,M\sqrt{\psi_0(\varepsilon_1)} + B\Big) \\
&= \lambda\,\psi_{\mathrm{cond}}(\varepsilon_1) + (1-\lambda)\,\psi_{\mathrm{cond}}(\varepsilon_2),
\end{aligned} \tag{C.42}$$

which was to be shown (C.33).

C.4. Existence of minimizers to mechanical mixed boundary-value problems

The purpose of this Appendix is to provide arguments for the validity of property (iii) listed in Section 3.3, i.e., the existence of a minimizer $\boldsymbol{u} \in H^1_D(\Omega)^n$ to the problem (3.37)

$$\mathcal{F}(\boldsymbol{u}) := \int_\Omega \psi_{\mathrm{cond}}(\nabla^s(\boldsymbol{u}_0 + \boldsymbol{u})) + \boldsymbol{f}\cdot\boldsymbol{u}\;\mathrm{d}V + \int_{\Gamma_N} \boldsymbol{t}\cdot\boldsymbol{u}\;\mathrm{d}A \longrightarrow \min_{\boldsymbol{u}\in H^1_D(\Omega)^n}. \tag{C.43}$$

The key properties required for establishing the validity of this statement are the bounds (3.33)

$$c_-\,\|\varepsilon\|^2 \le \psi_{\mathrm{cond}}(\varepsilon) \le C_+ + c_+\,\|\varepsilon\|^2, \quad \varepsilon \in \mathrm{Sym}(n), \tag{C.44}$$

valid with constants $c_\pm$ and C_+ independent of the strain and the convexity of the condensed incremental energy ψ_{cond}. Then, the existence of minimizers for the function $\mathcal{F}$ follow from standard arguments, more precisely the direct method in the calculus of variations. Let $(\boldsymbol{u}_k)$ be a minimizing sequence in $H^1_D(\Omega)^n$, i.e.,

$$\lim_{k\to\infty} \mathcal{F}(\boldsymbol{u}_k) = \mathcal{F}^* \equiv \min_{\boldsymbol{u}\in H^1_D(\Omega)^n} \mathcal{F}(\boldsymbol{u}). \tag{C.45}$$

The lower bound (C.43) implies the inequality

$$\int_\Omega c_- \|\nabla^s(\boldsymbol{u}_0+\boldsymbol{u})\|^2 + \boldsymbol{f}\cdot\boldsymbol{u}\,\mathrm{d}V + \int_{\Gamma_N} \boldsymbol{t}\cdot\boldsymbol{u}\,\mathrm{d}A \le \mathcal{F}(\boldsymbol{u}), \quad \boldsymbol{u}\in H^1_D(\Omega)^n, \tag{C.46}$$

or, put differently

$$\|\nabla^s(\boldsymbol{u}_0+\boldsymbol{u})\|^2_{H^1_D(\Omega)^n} \le C\left[\mathcal{F}(\boldsymbol{u}) + \left(\|\boldsymbol{f}\|_{H_D^{-1}(\Omega)^n} + \|\boldsymbol{t}\|_{H_D^{-\frac{1}{2}}(\Gamma_N)^n}\right)\|\nabla^s(\boldsymbol{u}_0+\boldsymbol{u})\|_{H^1_D(\Omega)^n}\right] \tag{C.47}$$

for some constant C independent of $\boldsymbol{u}\in H^1_D(\Omega)^n$. As a consequence of the definition (C.45), the sequence $(\boldsymbol{u}_k)$ is uniformly bounded in $H^1_D(\Omega)^n$. By the weak compactness of bounded sets in Hilbert spaces, there is a limit $\boldsymbol{u}^*\in H^1_D(\Omega)^n$, s.t., possibly up to selecting a subsequence, the sequence $(\boldsymbol{u}_k)$ converges weakly to $\boldsymbol{u}^*$, i.e.,

$$\boldsymbol{u}_k \to \boldsymbol{u}^* \text{ strongly in } L^2(\Omega)^n, \tag{C.48}$$

$$\nabla\boldsymbol{u}_k \rightharpoonup \nabla\boldsymbol{u}^* \text{ weakly in } L^2(\Omega)^{n\times n}. \tag{C.49}$$

As integral functionals with convex integrands satisfying the upper bound (C.43) are weakly lower semicontinuous in L^2, see, e.g., Dacorogna [62], we deduce

$$\mathcal{F}(\boldsymbol{u}^*) \le \liminf_{k\to\infty} \mathcal{F}(\boldsymbol{u}) \equiv \mathcal{F}^* \equiv \min_{\boldsymbol{u}\in H^1_D(\Omega)^n} \mathcal{F}(\boldsymbol{u}) \tag{C.50}$$

where we used the construction (C.45). In particular, $\boldsymbol{u}^*\in H^1_D(\Omega)^n$ represents the sought minimizer.

References

[1] S. Murakami, Continuum Damage Mechanics, 185 of *Solid Mechanics and Its Applications*, Springer Netherlands, Dordrecht, Dordrecht, 2012.
[2] A. Menzel, Continuum damage mechanics—modelling and simulation, in: Constitutive Modelling of Solid Continua, 262, Springer International Publishing, Cham, 2020, pp. 231–256.
[3] L.M. Kachanov, Rupture time under creep conditions, Int. J. Fract. 97 (1–4) (1999) 11–18.
[4] Y.N. Rabotnov, On the equation of state of creep, Proc. Inst. Mech. Eng. Conf. Proc. 178 (1) (1963) 2–117.
[5] J. Lemaitre, A Course on Damage Mechanics, Springer, Berlin, 2nd edition, Berlin, 1996.
[6] G. Li, C.A. Tang, A statistical meso-damage mechanical method for modeling trans-Scale progressive failure process of rock, Int. J. Rock Mech. Min. Sci. 74 (2015) 133–150.
[7] D. Krajcinovic, Damage mechanics, Mech. Mater. 8 (2–3) (1989) 117–197.
[8] Y. Liu, B. Sun, T. Guo, Z. Li, Multiscale damage analysis of engineering structures from material level to structural level: a systematic review, Int. J. Struct. Integr. 16 (2) (2025) 275–310.
[9] J. Fitoussi, N. Bourgeois, G. Guo, D. Baptiste, Prediction of the anisotropic damaged behavior of composite materials: introduction of multilocal failure criteria in a micro-macro relationship, Comput. Mater. Sci 5 (1–3) (1996) 87–100.
[10] G. Guo, J. Fitoussi, D. Baptiste, N. Sicot, C. Wolff, Modelling of damage behaviour of a short-fiber reinforced composite structure by the finite element analysis using a micro-macro law, Int. J. Damage Mech. 6 (3) (1997) 278–299.
[11] N. Weigel, D. Dinkler, B.H. Kröplin, Micromechanically based continuum damage mechanics material laws for fiber-Reinforced ceramics, Comput. Struct. 79 (22–25) (2001) 2277–2286.
[12] J.W. Ju, Y. Wu, Stochastic micromechanical damage modeling of progressive fiber breakage for longitudinal fiber-reinforced composites, Int. J. Damage Mech. 25 (2) (2016) 203–227.
[13] Y. Wu, J.W. Ju, Elastoplastic damage micromechanics for continuous fiber-reinforced ductile matrix composites with progressive fiber breakage, Int. J. Damage Mech. 26 (1) (2017) 4–28.
[14] X. Li, X. Qu, C. Qi, Z. Shao, An analytical model of multi-stress drops triggered by localized microcrack damage in brittle rocks during progressive failure, Int. J. Damage Mech. 29 (9) (2020) 1345–1360.
[15] V. Tojaga, A. Prapavesis, J. Faleskog, T.C. Gasser, A.W. Van Vuure, S. Östlund, Continuum damage micromechanics description of the compressive failure mechanisms in sustainable biocomposites and experimental validation, J. Mech. Phys. Solids 171 (2023) 105138.
[16] J. Lemaitre, A continuous damage mechanics model for ductile fracture, J. Eng. Mater. Technol. 107 (1) (1985) 83–89.
[17] J.C. Simo, J.W. Ju, Strain- and stress-based continuum damage models—I. formulation, Int. J. Solids Struct. 23 (7) (1987) 821–840.
[18] J.L. Chaboche, Continuum damage mechanics: part i—general concepts, J. Appl. Mech. 55 (1) (1988) 59–64.
[19] N.R. Hansen, H.L. Schreyer, A thermodynamically consistent framework for theories of elastoplasticity coupled with damage, Int. J. Solids Struct. 31 (3) (1994) 359–389.
[20] M. Brünig, A. Michalski, A stress-state-dependent continuum damage model for concrete based on irreversible thermodynamics, Int. J. Plast. 90 (2017) 31–43.
[21] P. Wriggers, S.O. Moftah, Mesoscale models for concrete: homogenisation and damage behaviour, Finite Elem. Anal. Des. 42 (7) (2006) 623–636.
[22] J. Görthofer, M. Schneider, A. Hrymak, T. Böhlke, A convex anisotropic damage model based on the compliance tensor, Int. J. Damage Mech. 31 (1) (2022) 43–86.
[23] W.C. Zhu, C.A. Tang, Micromechanical model for simulating the fracture process of rock, Rock Mech. Rock Eng. 37 (1) (2004) 25–56.
[24] G.Z. Voyiadjis, P.I. Kattan, A comparative study of damage variables in continuum damage mechanics, Int. J. Damage Mech. 18 (4) (2009) 315–340.
[25] W.-S. Li, J.Y. Wu, A consistent and efficient localized damage model for concrete, Int. J. Damage Mech. 27 (4) (2018) 541–567.
[26] D. Liu, M. He, M. Cai, A damage model for modeling the complete stress–strain relations of brittle rocks under uniaxial compression, Int. J. Damage Mech. 27 (7) (2018) 1000–1019.
[27] H. Yan, H. Jin, R. Yao, Prediction of the damage and fracture of cast steel containing pores, Int. J. Damage Mech. 29 (1) (2020) 166–183.
[28] G. Abu-Farsakh, A. Asfa, A unified damage model for fibrous composite laminae subject to in-plane stress-state and having multi material-nonlinearity, Int. J. Damage Mech. 29 (9) (2020) 1329–1344.
[29] Y. Song, J. Yeon, G.Z. Voyiadjis, Theoretical and numerical modeling of the effect of damage and dynamic strain aging on the plastic response of C45 steel alloys, Int. J. Damage Mech. 34 (5) (2024) 736–755.
[30] C.L. Chow, J. Wang, An anisotropic theory of elasticity for continuum damage mechanics, Int. J. Fract. 33 (1) (1987) 3–16.
[31] S. Murakami, Mechanical modeling of material damage, J. Appl. Mech. 55 (2) (1988) 280–286.
[32] J.L. Chaboche, Development of continuum damage mechanics for elastic solids sustaining anisotropic and unilateral damage, Int. J. Damage Mech. 2 (4) (1993) 311–329.
[33] S. Onodera, T. Okabe, Analytical model for determining effective stiffness and mechanical behavior of polymer matrix composite laminates using continuum damage mechanics, Int. J. Damage Mech. 29 (10) (2020) 1512–1542.

[34] J.L. Chaboche, Continuous damage mechanics — A tool to describe phenomena before crack initiation, Nucl. Eng. Des. 64 (2) (1981) 233–247.
[35] L. Olsen-Kettle, Using ultrasonic investigations to develop anisotropic damage models for initially transverse isotropic materials undergoing damage to remain transverse isotropic, Int. J. Solids Struct. 138 (2018) 155–165.
[36] L. Olsen-Kettle, Quantifying the orthotropic damage tensor for composites undergoing damage-induced anisotropy using ultrasonic investigations, Compos. Struct. 204 (2018) 701–711.
[37] G.Z. Voyiadjis, P.I. Kattan, Advances in Damage Mechanics: Metals and Metal Matrix Composites With an Introduction to Fabric Tensors, Elsevier Science, Burlington, 2nd edition, Burlington, 2010.
[38] J. Lemaitre, Local approach of fracture, Eng. Fract. Mech. 25 (5–6) (1986) 523–537.
[39] R. De Borst, L.J. Sluys, H.-B. Muhlhaus, J. Pamin, Fundamental issues in finite element analyses of localization of deformation, Eng. Comput. 10 (2) (1993) 99–121.
[40] S. Forest, E. Lorentz, Localization phenomena and regularization methods, in: Local Approach to Fracture, École des Mines de Paris, Paris, 2004, pp. 311–371.
[41] A. Needleman, Material rate dependence and mesh sensitivity in localization problems, Comput. Methods Appl. Mech. Eng. 67 (1) (1988) 69–85.
[42] L.J. Sluys, R. De Borst, Wave propagation and localization in a rate-dependent cracked medium—model formulation and one-dimensional examples, Int. J. Solids Struct. 29 (23) (1992) 2945–2958.
[43] J.-F. Dubé, G. Pijaudier-Cabot, C.L. Borderie, Rate dependent damage model for concrete in dynamics, J. Eng. Mech. 122 (10) (1996) 939–947.
[44] G. Pijaudier-Cabot, Z.P. Bažant, Nonlocal damage theory, J. Eng. Mech. 113 (10) (1987) 1512–1533.
[45] W.K. Liu, S. Hao, T. Belytschko, S. Li, C.T. Chang, Multiple scale meshfree methods for damage fracture and localization, Comput. Mater. Sci 16 (1–4) (1999) 197–205.
[46] Z.P. Bažant, M. Jirásek, Nonlocal integral formulations of plasticity and damage: survey of progress, J. Eng. Mech. 128 (11) (2002) 1119–1149.
[47] E. Lorentz, S. Andrieux, Analysis of non-local models through energetic formulations, Int. J. Solids Struct. 40 (12) (2003) 2905–2936.
[48] R.H.J. Peerlings, R. De Borst, W.A.M. Brekelmans, J.H.P. De Vree, Gradient enhanced damage for quasi-brittle materials, Int. J. Numer. Methods Eng. 39 (19) (1996) 3391–3403.
[49] M. Brünig, S. Ricci, Nonlocal continuum theory of anisotropically damaged metals, Int. J. Plast. 21 (7) (2005) 1346–1382.
[50] R.K. Abu Al-Rub, G.Z. Voyiadjis, Gradient-enhanced coupled plasticity-anisotropic damage model for concrete fracture: computational aspects and applications, Int. J. Damage Mech. 18 (2) (2009) 115–154.
[51] B.J. Dimitrijevic, K. Hackl, A regularization framework for damage-plasticity models via gradient enhancement of the free energy, Int. J. Numer. Method Biomed. Eng. 27 (8) (2011) 1199–1210.
[52] Y. Navidtehrani, C. Betegón, E. Martínez-Pañeda, A simple and robust abaqus implementation of the phase field fracture method, Appl. Eng. Sci. 6 (2021) 100050.
[53] F. Ernesti, M. Schneider, A fast fourier transform based method for computing the effective crack energy of a heterogeneous material on a combinatorially consistent grid, Int. J. Numer. Methods Eng. 122 (21) (2021) 6283–6307.
[54] W.J. Drugan, J.R. Willis, A micromechanics-based nonlocal constitutive equation and estimates of representative volume element size for elastic composites, J. Mech. Phys. Solids 44 (4) (1996) 497–524.
[55] T. Kanit, S. Forest, I. Galliet, V. Mounoury, D. Jeulin, Determination of the size of the representative volume element for random composites: statistical and numerical approach, Int. J. Solids Struct. 40 (13–14) (2003) 3647–3679.
[56] I.M. Gitman, H. Askes, L.J. Sluys, Representative volume: existence and size determination, Eng. Fract. Mech. 74 (16) (2007) 2518–2534.
[57] D. Balzani, M. Ortiz, Relaxed incremental variational formulation for damage at large strains with application to fiber-reinforced materials and materials with truss-like microstructures, Int. J. Numer. Methods Eng. 92 (6) (2012) 551–570.
[58] T. Schmidt, D. Balzani, Relaxed incremental variational approach for the modeling of damage-induced stress hysteresis in arterial walls, J. Mech. Behav. Biomed. Mater. 58 (2016) 149–162.
[59] S. Schwarz, P. Junker, K. Hackl, Variational regularization of damage models based on the emulated RVE, Continuum Mech. Thermodyn. 33 (1) (2021) 69–95.
[60] D. Balzani, M. Köhler, T. Neumeier, M.A. Peter, D. Peterseim, Multidimensional rank-one convexification of incremental damage models at finite strains, Comput. Mech. 73 (1) (2024) 27–47.
[61] C.B. Morrey, Quasi-convexity and the lower semicontinuity of multiple integrals, Pac. J. Math. 2 (1) (1952) 25–53.
[62] B. Dacorogna, Quasiconvexity and relaxation of nonconvex problems in the calculus of variations, J. Funct. Anal. 46 (1) (1982) 102–118.
[63] O. Allix, The bounded rate concept: a framework to deal with objective failure predictions in dynamic within a local constitutive model, Int. J. Damage Mech. 22 (6) (2013) 808–828.
[64] F. Feyel, Multiscale FE2 elastoviscoplastic analysis of composite structures, Comput. Mater. Sci. 16 (1–4) (1999) 344–354.
[65] F. Feyel, J.L. Chaboche, FE2 Multiscale approach for modelling the elastoviscoplastic behaviour of long fibre SiC/Ti composite materials, Comput. Methods Appl. Mech. Eng. 183 (3–4) (2000) 309–330.
[66] F. Feyel, A multilevel finite element method (FE2) to describe the response of highly non-Linear structures using generalized continua, Comput. Methods Appl. Mech. Eng. 192 (28–30) (2003) 3233–3244.
[67] J. Spahn, H. Andrä, M. Kabel, R. Müller, A multiscale approach for modeling progressive damage of composite materials using fast fourier transforms, Comput. Methods Appl. Mech. Eng. 268 (2014) 871–883.
[68] J. Kochmann, S. Wulfinghoff, S. Reese, J.R. Mianroodi, B. Svendsen, Two-scale FE–FFT- and phase-field-based computational modeling of bulk microstructural evolution and macroscopic material behavior, Comput. Methods Appl. Mech. Eng. 305 (2016) 89–110.
[69] I. Fonseca, D. Kinderlehrer, P. Pedregal, Energy functional depending on elastic strain and chemical composition, Calc. Var. Partial Differ. Equations 2 (3) (1994) 283–313.
[70] H. Le Dret, A. Raoult, Variational convergence for nonlinear shell models with directors and related semicontinuity and relaxation results, Arch. Ration. Mech. Anal. 154 (2) (2000) 101–134.
[71] C. Carstensen, K. Hackl, A. Mielke, Non–convex potentials and microstructures in finite–strain plasticity, Proc. R. Soc. London Ser. A Math. Phys. Eng. Sci. 458 (2018) (2002) 299–317.
[72] M. Köhler, D. Balzani, Evolving microstructures in relaxed continuum damage mechanics for the modeling of strain softening, J. Mech. Phys. Solids 173 (2023) 105199.
[73] J. Melchior, M. Köhler, D. Balzani, Variationally consistent microstructure evolution and microsphere-based reconvexification for damage with application to arterial tissues, Mech. Mater. 212 (2026) 105495.
[74] C. Villani, Optimal Transport, 338 of *Grundlehren Der Mathematischen Wissenschaften*, Springer, Berlin, Heidelberg, Berlin, Heidelberg, 2009.
[75] H. Moulinec, P. Suquet, A fast numerical method for computing the linear and nonlinear mechanical properties of composites, C. R. de l'Acad. des Sci. Ser. II 318 (11) (1994) 1417–1423.
[76] H. Moulinec, P. Suquet, A numerical method for computing the overall response of nonlinear composites with complex microstructure, Comput. Methods Appl. Mech. Eng. 157 (1–2) (1998) 69–94.
[77] M. Schneider, A review of nonlinear FFT-based computational homogenization methods, Acta Mech. 232 (6) (2021) 2051–2100.
[78] B. Halphen, Q.S. Nguyen, Sur les matériaux standard généralisés, J. Mécanique 14 (1) (1975) 39–63.
[79] Q.S. Nguyen, Stability and Nonlinear Solid Mechanics, Wiley, New York, New York, 2000.
[80] T. Brepols, S. Wulfinghoff, S. Reese, Gradient-extended two-surface damage-plasticity: micromorphic formulation and numerical aspects, Int. J. Plast. 97 (2017) 64–106.
[81] J.-Y. Wu, V.P. Nguyen, A length scale insensitive phase-field damage model for brittle fracture, J. Mech. Phys. Solids 119 (2018) 20–42.
[82] P. Haupt, Continuum Mechanics and Theory of Materials, Advanced Texts in Physics, Springer, Berlin, Heidelberg, Berlin, Heidelberg, 2002.
[83] M.A. Biot, Mechanics of Incremental Deformations, Wiley, New York, New York, 1965.

[84] R.T. Rockafellar, Convex Analysis, Princeton University Press, Princeton, Princeton, 1970.
[85] M. Ortiz, L. Stainier, The variational formulation of viscoplastic constitutive updates, Comput. Methods Appl. Mech. Eng. 171 (3–4) (1999) 419–444.
[86] C. Miehe, Strain-driven homogenization of inelastic microstructures and composites based on an incremental variational formulation, Int. J. Numer. Methods Eng. 55 (11) (2002) 1285–1322.
[87] M. Köhler, T. Neumeier, M.A. Peter, D. Peterseim, D. Balzani, Hierarchical rank-one sequence convexification for the relaxation of variational problems with microstructures, Comput. Methods Appl. Mech. Eng. 432 (2024) 117321.
[88] B. Dacorogna, Direct Methods in the Calculus of Variations, number 78 in Applied Mathematical Sciences, Springer Science + Business Media, Luxemburg, 2nd edition, Luxemburg, 2008.
[89] C. Carathéodory, Über den variabilitätsbereich der Fourier'schen Konstanten von positiven harmonischen Funktionen, Rend. Circ. Mat. Palermo 32 (1) (1911) 193–217.
[90] C. Mittelstedt, Engineering Mechanics 3: Dynamics, Springer, Berlin, Berlin, 2025.
[91] G.A. Francfort, J.J. Marigo, Stable damage evolution in a brittle continuous medium, Eur. J. Mech. A/Solids 12 (2) (1993) 149–189.
[92] G.A. Francfort, A. Garroni, A variational view of partial brittle damage evolution, Arch. Ration. Mech. Anal. 182 (2006) 125–152.
[93] F. Santambrogio, Optimal Transport for Applied Mathematicians: Calculus of Variations, PDEs, and Modeling, Progress in Nonlinear Differential Equations and Their Applications, Springer International Publishing, Cham, Cham, 2015.
[94] L.V. Kantorovich, On the translocation of masses, J. Math. Sci. 133 (4) (2006) 1381–1382.
[95] N. Nocedal, J.W. Wright, Numerical Optimization, Springer Series in Operations Research and Financial Engineering, Springer Science + Business Media, Luxemburg, Luxemburg, 2006.
[96] D. Gross, T. Seelig, Fracture Mechanics: With an Introduction to Micromechanics, Mechanical Engineering Series, Springer International Publishing, Cham, Cham, 2018.
[97] M. Schneider, On the Barzilai-Borwein basic scheme in FFT-based computational homogenization, Int. J. Numer. Methods Eng. 118 (8) (2019) 482–494.
[98] M. Schneider, D. Wicht, T. Böhlke, On polarization-based schemes for the FFT-based computational homogenization of inelastic materials, Comput. Mech. 64 (4) (2019) 1073–1095.
[99] M. Schneider, F. Ospald, M. Kabel, Computational homogenization of elasticity on a staggered grid, Int. J. Numer. Methods Eng. 105 (9) (2016) 693–720.
[100] J. Zeman, J. Vondřejc, J. Novák, I. Marek, Accelerating a FFT-based solver for numerical homogenization of periodic media by conjugate gradients, J. Comput. Phys. 229 (21) (2010) 8065–8071.
[101] S. Brisard, L. Dormieux, Combining Galerkin approximation techniques with the principle of Hashin and Shtrikman to derive a new FFT-based numerical method for the homogenization of composites, Comput. Methods Appl. Mech. Eng. 217–220 (2012) 197–212.
[102] D. Wicht, M. Schneider, T. Böhlke, On quasi-Newton methods in fast fourier transform-based micromechanics, Int. J. Numer. Methods Eng. 121 (8) (2020) 1665–1694.
[103] M. Schneider, A dynamical view of nonlinear conjugate gradient methods with applications to FFT-based computational micromechanics, Comput. Mech. 66 (1) (2020) 239–257.
[104] I. Doghri, L. Brassart, L. Adam, J.S. Gérard, A second-moment incremental formulation for the mean-field homogenization of elasto-plastic composites, Int. J. Plast. 27 (3) (2011) 352–371.
[105] C. Lauff, M. Schneider, J. Montesano, T. Böhlke, Generating microstructures of long fiber reinforced composites by the fused sequential addition and migration method, Int. J. Numer. Methods Eng. 125 (22) (2024) e7573.
[106] C. Lauff, M. Krause, M. Schneider, T. Böhlke, On the influence of the fiber curvature on the stiffness of long fiber reinforced composites, Int. J. Numer. Methods Eng. 126 (15) (2025) e70094.
[107] J.K. Bauer, M. Schneider, T. Böhlke, On the phase space of fourth-order fiber-orientation tensors, J. Elast. 153 (2) (2023) 161–184.
[108] S. Montgomery-Smith, W. He, D.A. Jack, D.E. Smith, Exact tensor closures for the three-dimensional jeffery's equation, J. Fluid Mech. 680 (2011) 321–335.
[109] S. Montgomery-Smith, D.A. Jack, D.E. Smith, The fast exact closure for jeffery's equation with diffusion, J. Non-Newtonian Fluid Mech. 166 (7–8) (2011) 343–353.
[110] R. Hill, Elastic properties of reinforced solids: some theoretical principles, J. Mech. Phys. Solids 11 (5) (1963) 357–372.
[111] K. Sab, B. Nedjar, Periodization of random media and representative volume element size for linear composites, Compt. Rendus. Mécanique 333 (2) (2005) 187–195.
[112] M. Schneider, M. Josien, F. Otto, Representative volume elements for matrix-inclusion composites - a computational study on the effects of an improper treatment of particles intersecting the boundary and the benefits of periodizing the ensemble, J. Mech. Phys. Solids 158 (2022) 104652.
[113] M. Schneider, An algorithm for generating microstructures of fiber-reinforced composites with long fibers, Int. J. Numer. Methods Eng. 123 (24) (2022) 6197–6219.
[114] A. Gloria, F. Otto, An optimal variance estimate in stochastic homogenization of discrete elliptic equations, Ann. Probab. 39 (3) (2011) 779–856.
[115] A. Mehta, M. Schneider, A sequential addition and migration method for generating microstructures of short fibers with prescribed length distribution, Comput. Mech. 70 (4) (2022) 829–851.
[116] A. Puck, H. Schürmann, Failure analysis of FRP laminates by means of physically based phenomenological models, Compos. Sci. Technol. 62 (12–13) (2002) 1633–1662.
[117] M. Knops, A. Puck, Analysis of Failure in Fiber Polymer Laminates: The Theory of Alfred Puck, Springer, Berlin, Berlin, 2008.
[118] H. Rolland, N. Saintier, G. Robert, Damage mechanisms in short glass fibre reinforced thermoplastic during in situ microtomography tensile tests, Compos. Part B Eng. 90 (2016) 365–377.
[119] I. Hanhan, M.D. Sangid, Damage propagation in short fiber thermoplastic composites analyzed through coupled 3D experiments and simulations, Compos. Part B Eng. 218 (2021) 108931.
[120] N. Magino, J. Köbler, H. Andrä, F. Welschinger, R. Müller, M. Schneider, A multiscale high-cycle fatigue-damage model for the stiffness degradation of fiber-reinforced materials based on a mixed variational framework, Comput. Methods Appl. Mech. Eng. 388 (2022) 114198.
[121] N. Magino, J. Köbler, H. Andrä, F. Welschinger, R. Müller, M. Schneider, A space-time upscaling technique for modeling high-cycle fatigue-damage of short-fiber reinforced composites, Compos. Sci. Technol. 222 (2022) 109340.
[122] N. Magino, J. Köbler, H. Andrä, F. Welschinger, R. Müller, M. Schneider, Accounting for viscoelastic effects in a multiscale fatigue model for the degradation of the dynamic stiffness of short-fiber reinforced thermoplastics, Comput. Mech. 71 (3) (2023) 493–515.
[123] A. Braides, Homogenization of some almost periodic coercive functional, Rend. della Accad. Naz. Sci. 103 (1985) 313–322.
[124] S. Müller, Homogenization of nonconvex integral functionals and cellular elastic materials, Arch. Ration. Mech. Anal. 99 (3) (1987) 189–212.
[125] J.-C. Michel, P. Suquet, Merits and limits of a variational definition of the effective toughness of heterogeneous materials, J. Mech. Phys. Solids 164 (2022) 104889.
[126] M.Z. Hossain, C.-J. Hsueh, B. Bourdin, K. Bhattacharya, Effective toughness of heterogeneous media, J. Mech. Phys. Solids 71 (2014) 15–32.
[127] M. Schneider, An FFT-based method for computing weighted minimal surfaces in microstructures with applications to the computational homogenization of brittle fracture, Int. J. Numer. Methods Eng. 121 (7) (2020) 1367–1387.
[128] J. Köbler, N. Magino, H. Andrä, F. Welschinger, R. Müller, M. Schneider, A computational multi-scale model for the stiffness degradation of short-fiber reinforced plastics subjected to fatigue loading, Comput. Methods Appl. Mech. Eng. 373 (2021) 113522.
[129] N. Meyer, S. Gajek, J. Görthofer, A. Hrymak, L. Kärger, F. Henning, M. Schneider, T. Böhlke, A probabilistic virtual process chain to quantify process-induced uncertainties in sheet molding compounds, Compos. Part B Eng. 249 (2023) 110380.
[130] A.P. Dey, F. Welschinger, M. Schneider, J. Köbler, T. Böhlke, On the effectiveness of deep material networks for the multi-scale virtual characterization of short fiber-reinforced thermoplastics under highly nonlinear load cases, Arch. Appl. Mech. 94 (5) (2024) 1177–1202.
[131] J. Solomon, Optimal transport on discrete domains, AMS Short Course Discrete Diff. Geom. 3 (2018) 1–38.